

# Cosmic Evolution of Quasar Clustering: Implications for the Host Haloes

Cristiano Porciani<sup>1</sup>, Manuela Magliocchetti<sup>2</sup>, Peder Norberg<sup>1</sup>

<sup>1</sup> *Institute for Astronomy, HPPF G3.1, ETH Hönggerberg, 8093 Zürich, Switzerland*

<sup>2</sup> *SISSA, Via Beirut 4, 34014, Trieste, Italy*

16 March 2019

## ABSTRACT

We present detailed clustering measurements from the 2dF QSO Redshift Survey (2QZ) in the redshift range  $0.8 < z < 2.1$ . Using a flux limited sample of  $\sim 14,000$  objects with effective redshift  $z_{\text{eff}} = 1.47$ , we estimate the quasar projected correlation function for separations  $1 < r/h^{-1}\text{Mpc} < 20$ . We find that the 2-point correlation function in real space is well approximated by a power law with slope  $\gamma = 1.5 \pm 0.2$  and comoving correlation length  $r_0 = 4.8_{-1.5}^{+0.9} h^{-1}\text{Mpc}$ . Splitting the sample into three subsets based on redshift, we find evidence for an increase of the clustering amplitude with lookback time. For a fixed  $\gamma$ , evolution of  $r_0$  is detected at the  $3.6\sigma$  confidence level. The ratio between the quasar correlation function and the mass autocorrelation function (derived adopting the concordance cosmological model) is found to be scale independent. For a linear mass-clustering amplitude  $\sigma_8 = 0.8$ , the “bias parameter” decreases from  $b \simeq 3.9$  at  $z_{\text{eff}} = 1.89$  to  $b \simeq 1.8$  at  $z_{\text{eff}} = 1.06$ . From the observed clustering, we use three approaches to infer how quasars populate dark-matter haloes of different masses. Independently of the details of the assumed model, we find that 2QZ quasars sit in haloes with  $M > 10^{12}M_{\odot}$  and that the mean mass of their host haloes has to be a few  $\times 10^{13}M_{\odot}$ . The observed clustering is consistent with assuming that the locally observed correlation between black-hole mass and host-galaxy circular velocity is still valid at  $z > 1$ . From the fraction of haloes which contain active quasars, we infer that the characteristic quasar lifetime is  $t_{\text{Q}} \sim$  a few  $\times 10^7$  yr at  $z \sim 1$  and approaches  $10^8$  yr at higher redshifts.

**Key words:** galaxies: active - galaxies: clustering - quasars: general - cosmology: theory - large-scale structure - cosmology: observations

## 1 INTRODUCTION

Recent dynamical studies have provided strong evidence for the existence of supermassive black holes in the centre of most nearby galaxies (for a review, see e.g. Richstone et al. 1998). The mass of the central black hole seems to correlate with the luminosity and the velocity dispersion of the spheroidal stellar component (e.g. Magorrian et al. 1998; Gebhardt et al. 2000; Ferrarese & Merritt 2000; Tremaine et al. 2002). The surprising tightness of the latter relation suggests the existence of a strong connection between the formation of supermassive black holes and the assembly of galactic spheroids (Silk & Rees 1998; Haehnelt & Kauffmann 2000; Kauffmann & Haehnelt 2000; Monaco, Salucci & Danese 2000; Granato et al. 2004).

The mounting evidence for the presence of supermassive black holes in nearby galaxies supports the theoretical belief that quasars are powered by black-hole accretion (Salpeter 1964; Zel’dovich & Novikov 1964; Lynden-Bell 1969). For instance, the locally estimated mass density in black holes

and the observed evolution of the quasar luminosity function seem to be consistent with this picture (Haehnelt, Natarajan, Rees 1998; Fabian & Iwasawa 1999; Salucci et al. 1999; Yu & Tremaine 2002; Wyithe & Loeb 2003; Marconi et al. 2004). A detailed understanding of the physical processes leading to quasar activity (and their connection with galaxy formation) is still lacking. For this reason, even simple phenomenological models which are able to reproduce the observational results by selecting which cosmic structures could harbour quasars are of paramount importance.

In the currently favoured cosmological model, galaxies are expected to form within extended dark-matter haloes. At every epoch, the number density and clustering properties of the haloes can be readily (and reliably) computed as a function of their mass. It is therefore of great interest to try to establish a connection between these haloes and different classes of cosmic objects. A number of “halo models” have been presented in the literature. These have been successfully used to describe the clustering and abun-

dance properties of galaxies at both low (Peacock & Smith 2000; Seljak 2000; Scoccimarro et al. 2001; Marinoni & Hudson 2002; Berlind & Weinberg 2001; Yang, Mo & van den Bosch 2003; van den Bosch, Yang & Mo 2003; Zehavi et al. 2003; Magliocchetti & Porciani 2003) and high (Bullock, Wechsler & Somerville 2002; Moustakas & Somerville 2002; Zheng 2004) redshift.

In order to apply the halo model to the population of optically selected quasars one first needs to accurately determine their mean abundance and clustering properties. Since the first detection of quasar clustering, (Shaver 1984; Shanks et al. 1987), a number of surveys (continuously improved in terms of homogeneity, completeness and size) have been used to measure the quasar 2-point correlation function (Iovino & Shaver 1988; Andreani & Cristiani 1992; Mo & Fang 1993; Shanks & Boyle 1994; Andreani et al. 1994; Croom & Shanks 1996; La Franca, Andreani & Cristiani 1998; Grazian et al. 2004). The emerging picture is that quasars at  $z \sim 1.5$  have a correlation length of  $5 - 6 h^{-1}$  Mpc, similar to that of present-day galaxies. It still is a matter of debate, however, whether  $r_0$  significantly evolves with redshift (Iovino & Shaver 1988; Croom & Shanks 1996; La Franca, Andreani & Cristiani 1998). This uncertainty is due to the joint effects of cosmic variance and small-number statistics: given the sparseness of the quasar distribution, a typical sample includes from a few-hundred to a thousand objects. In consequence, clustering is generally detected at a relatively low significance level ( $3 - 4\sigma$ ).

The development of efficient multi-object spectrographs has recently made possible a new generation of wide-area redshift surveys. Both the completed Two-degree Field (2dF) QSO Redshift Survey (Croom et al. 2004) and the on-going Sloan Digital Sky Survey (SDSS) Quasar Survey (Schneider et al. 2003) list redshifts for tens of thousands of optically selected quasars. A preliminary data release of the 2QZ has been used to estimate the evolution and the luminosity dependence of the quasar 2-point correlation function in redshift-space (Croom et al. 2001; 2002). The final catalogue has been employed to measure the quasar power spectrum out to scales of  $500 h^{-1}$  Mpc (Outram et al. 2003; see also Hoyle et al. 2002) and to constrain the cosmological constant from redshift-space distortions (Outram et al. 2004).

In this paper, we study the clustering properties of  $\sim 14,000$  quasars extracted from the complete 2dF QSO Redshift Survey. In particular, we compute the projected 2-point correlation of quasars in three different redshift bins. This quantity is not affected by the distortion of the clustering pattern induced by peculiar motions as it measures the clustering strength as a function of quasar separation in the perpendicular direction to the line of sight. In the second part of this paper, we combine our state-of-the-art estimates of quasar clustering in real space with the halo model to infer the mean number of optically selected quasars which are harboured by a virialized halo of given mass (the halo occupation number) and the characteristic quasar lifetime. This is done employing three different methods which give consistent results. In brief, our results translate the observed quasar number density and clustering amplitude into a set of quantities which can be directly used to build (and/or test) physical models for black-hole accretion.

The layout of the paper is as follows. In Section 2.1,

we describe our quasar samples, for which we measure, in Sections 2.3-2.5, the projected correlation function, and estimate, in Section 2.7, the associated effective bias. The formalism of the halo model is introduced in Section 3.1. Three simple models for the quasar halo occupation number are presented in Section 3.3 where we discuss how the associated free parameters (2 for each model) are constrained by the data. Using the observed correlation between black-hole mass and circular velocity of the host galaxy (Ferrarese 2002; Baes et al. 2003), we derive, in Sections 4.1 and 4.2, the mass distribution of haloes that harbour quasars of a given  $b_J$ -band absolute magnitude. The corresponding halo occupation number is presented in Section 4.3 where we also compare model predictions for the clustering amplitude with observations. In Section 5, we introduce a more general model for the halo occupation number. Its three free parameters are constrained in Section 5.5, by using the results obtained in Section 4.1 as a Bayesian prior. The evolution of the halo occupation number over the redshift range  $0.8 < z < 2.1$  is addressed in Section 6. We discuss our results in Section 7 and conclude in Section 8.

Throughout this work, we assume that the mass density parameter  $\Omega_0 = 0.3$  (with a baryonic contribution  $\Omega_b = 0.049$ ), the vacuum energy density parameter  $\Omega_\Lambda = 0.7$  and the present-day value of the Hubble constant  $H_0 = 100 h \text{ km s}^{-1} \text{ Mpc}^{-1}$  with  $h = 0.7$ . We also adopt a cold dark matter power spectrum with primordial spectral index  $n = 1$  and  $\sigma_8 = 0.8$  (with  $\sigma_8$  the rms linear density fluctuation within a sphere with a radius of  $8 h^{-1}$  Mpc). This is consistent with the most recent joint-analyses of temperature anisotropies in the cosmic microwave background and galaxy clustering (see e.g. Tegmark et al. 2004 and references therein) and with the observed quasar power spectrum (Outram et al. 2003).

## 2 THE DATA

In this section, we present the main properties of our dataset and compute its clustering properties as a function of redshift.

### 2.1 Quasar selection and sample definitions

The 2dF QSO Redshift Survey (2QZ) is a homogeneous database containing the spectra of 44,576 stellar-like objects with  $18.25 \leq b_J \leq 20.85$  (Croom et al. 2004). Selection of the quasar candidates is based on broadband colours ( $ub_{1r}$ ) from APM measurements of UK Schmidt Telescope (UKST) photographic plates. Spectroscopic observations with the 2dF instrument (a multi-fibre spectrograph) at the Anglo-Australian Telescope have been used to determine the intrinsic nature of the sources. The full survey includes 23,338 quasars (the vast majority of which are endowed with a high-quality identification and/or redshift) which span a wide redshift range ( $0.3 \lesssim z \lesssim 2.9$ ) and are spread over  $721.6 \text{ deg}^2$  on the sky (see Croom et al. 2004 for further details).

The 2QZ is affected by incompleteness in a number of different ways (for a detailed discussion see Croom et al. 2004). In order to minimise systematic effects, we restrict our analysis to a sub-sample of sources defined by a min-

**Table 1.** Main properties of our datasets. The superscripts min, max and med respectively denote the minimum, the maximum and the median value of a variable.

$z_{\min}$	$z_{\max}$	$z_{\text{eff}}$	$M^{\min}$	$M^{\max}$	$M^{\text{med}}$	$N_{\text{QSO}}$	$n_{\text{QSO}}$ $10^{-6} h^3 \text{Mpc}^{-3}$	$b_{\text{J}}^{\text{med}}$
			$M_{b_{\text{J}}} - 5 \log_{10} h$					
0.8	1.3	1.06	-25.32	-21.72	-23.13	4928	$8.54 \pm 0.47 \pm 0.85$	19.95
1.3	1.7	1.51	-25.97	-22.80	-23.84	4737	$7.20 \pm 0.35 \pm 0.72$	20.02
1.7	2.1	1.89	-26.44	-23.37	-24.30	4324	$6.21 \pm 0.26 \pm 0.62$	20.07
0.8	2.1	1.47	-26.44	-21.72	-23.82	13989	$11.49 \pm 1.52 \pm 1.15$	20.02

imum spectroscopic sector completeness of 70 per cent.<sup>1</sup> Moreover, we only consider regions of the 2QZ catalogue for which the photometric completeness is greater than 90 per cent; this corresponds to a redshift range  $0.5 < z < 2.1$ . Finally, we impose a cut in absolute magnitude, so that we only consider quasars brighter than  $M_{b_{\text{J}}} - 5 \log_{10} h = -21.7$ , which, assuming  $h = 0.7$ , is equivalent to  $M_{b_{\text{J}}} = -22.5$ . Such an absolute magnitude cut ensures the exclusion of quasars where the contribution from the host galaxy may have led to a mis-identification of the source.

In order to detect possible evolutionary effects, we want to subdivide our sample into three redshift bins. In particular, we require that: (i) a similar number of quasars lies in each redshift bin, and (ii) each sub-sample covers a not too different interval of cosmic time. For this reason, we revise our initial sample selection by imposing an additional redshift cut, so to keep only objects within  $0.8 < z < 2.1$ . In fact, the time interval covered by the redshift range  $0.5 < z < 0.8$  (1.78 Gyr) corresponds to one third of the total time elapsed between  $z = 2.1$  and  $z = 0.5$  (5.35 Gyr), whereas the number of quasars with  $0.5 < z < 0.8$  represents less than 10 per cent of the selected quasar sample. By restricting the analysis to  $0.8 < z < 2.1$ , we can greatly improve on both the previously mentioned conditions. Moreover, we obtain a sample for which the mean number density of quasars is very weakly varying with redshift (as it can be seen in Fig. 1 of Outram et al. 2003), since through this cut we remove the largest mean number density variations as a function of redshift. The drop in mean density is less than 60 per cent between  $z = 0.8$  and  $z = 2.1$ . For this reason, in the calculation of the quasar correlation function, we ignore any weighting scheme which compensates for a varying mean density, like the standard  $J_3$ -type weighting usually needed when estimating the clustering from magnitude limited samples (Efstathiou 1988).

With the above selection, we end up with nearly 14,000 quasars (split in two regions – the north galactic pole strip (NGP) and the south galactic pole strip (SGP) – with respectively  $\sim 7800$  and  $\sim 6100$  quasars each), of which 75 per cent reside in regions with total completeness larger than 80 per cent. In order to study the evolution of quasar clustering, we divide this sample into three redshift slices. To satisfy our previously mentioned criteria, we end up choosing the following three intervals:  $0.8 < z < 1.3$ ,  $1.3 < z < 1.7$  and  $1.7 < z < 2.1$ , containing each between  $\sim 4300$  and  $\sim 4900$  quasars (see Table 1). We note that the time covered be-

tween  $z = 0.8$  and  $z = 1.3$  (1.91 Gyr) is nearly twice the time covered between  $z = 1.3$  and  $z = 1.7$  (0.97 Gyr); this is however unavoidable if we want to keep similar numbers of quasars in each redshift interval. As the sample is magnitude limited, each redshift interval will correspond to quasars of different intrinsic luminosities, a point we address further in Section 2.2.

## 2.2 Number densities of quasars

Croom et al. (2004) provide an analytical fit for the  $b_{\text{J}}$  quasar luminosity function, in the case of sources brighter than  $M_{b_{\text{J}}} - 5 \log_{10} h \geq -21.7$  and for  $0.4 < z < 2.1$ . They model the optical luminosity function as a double power law in luminosity which, as a function of magnitude (number of quasars per unit magnitude per unit volume), becomes

$$\Phi(M_{b_{\text{J}}}, z) = \frac{\Phi^*}{10^{0.4 \beta_1 (M_{b_{\text{J}}} - M_{b_{\text{J}}}^*)} + 10^{0.4 \beta_2 (M_{b_{\text{J}}} - M_{b_{\text{J}}}^*)}}, \quad (1)$$

where the evolution is encoded in the redshift dependence of the characteristic magnitude  $M_{b_{\text{J}}}^* \equiv M_{b_{\text{J}}}^*(z) = M_{b_{\text{J}}}^*(0) - 1.08 k \tau(z)$  with  $\tau(z)$  the fractional look-back time (in units of the present age of the Universe) at redshift  $z$  and  $k$  a constant. A table with the best-fitting values for the parameters  $\beta_1$ ,  $\beta_2$ ,  $M_{b_{\text{J}}}^*(0)$  and  $k$  is provided by Croom et al. (2004), together with their statistical uncertainties.

Equation (1) can be used to compute the selection function of the 2QZ between  $z_{\min} < z < z_{\max}$ :

$$S(z, z_{\min}, z_{\max}) = \frac{\int_{M_{b_{\text{J}}}^{\text{b}}(z)}^{M_{b_{\text{J}}}^{\text{f}}(z)} \Phi(M_{b_{\text{J}}}, z) dM_{b_{\text{J}}}}{\int_{M_{b_{\text{J}}}^{\text{min}}}^{M_{b_{\text{J}}}^{\text{max}}} \Phi(M_{b_{\text{J}}}, z) dM_{b_{\text{J}}}}, \quad (2)$$

where  $M_{b_{\text{J}}}^{\text{b}}(z)$  and  $M_{b_{\text{J}}}^{\text{f}}(z)$  denote, respectively, the brightest and faintest absolute magnitudes which are detectable at redshift  $z$ . These are obtained by using the K-correction from the composite quasar spectrum by Brotherton et al. (2001), and by assuming fixed apparent magnitude limits:  $b_{\text{J}}^{\text{faint}} = 18.25$  and  $b_{\text{J}}^{\text{bright}} = 20.85$ . The integration limits in the denominator of equation (2) are  $M_{b_{\text{J}}}^{\text{min}} = \min_{(z_{\min}, z_{\max})} M_{b_{\text{J}}}^{\text{b}}(z)$  and  $M_{b_{\text{J}}}^{\text{max}} = \max_{(z_{\min}, z_{\max})} M_{b_{\text{J}}}^{\text{f}}(z)$ . The comoving volume effectively surveyed is then given by

$$V_{\text{eff}}(z_{\min}, z_{\max}) = \Omega_{\text{s}} \int_{z_{\min}}^{z_{\max}} S(z, z_{\min}, z_{\max}) \left| \frac{dV}{dz d\Omega} \right| dz, \quad (3)$$

where  $\Omega_{\text{s}}$  denotes the solid angle covered by the survey and  $|dV/dz d\Omega|$  is the Jacobian determinant of the transformation between comoving and redshift-space coordinates, which gives the comoving volume element per unit redshift

<sup>1</sup> A sector is as a unique area on the sky defined by the intersection of a number of circular 2dF fields.

and solid angle. We can then estimate the mean number density of quasars by writing

$$n_{\text{QSO}}(z_{\text{min}}, z_{\text{max}}) = \sum_{i=1}^{N_{\text{QSO}}} \frac{w_i}{V_{\text{eff}}(z_{\text{min}}, z_{\text{max}})}, \quad (4)$$

where  $N_{\text{QSO}}$  and  $\sum_i w_i$  are, respectively, the total number of observed quasars in the range  $z_{\text{min}} < z < z_{\text{max}}$  and its completeness weighted counterpart. Results obtained by applying equation (4) are listed in Table 1, where we summarize the main properties of our samples. Two types of errors are quoted for  $n_{\text{QSO}}$ . Those listed first are determined by independently varying the four parameters which define the optical quasar luminosity function (i.e.  $\beta_1$ ,  $\beta_2$ ,  $M_{b_J}^*(0)$  and  $k$ ) within their  $1\sigma$  uncertainties as reported by Croom et al. (2004).<sup>2</sup> On top of this error, we quote a  $\sim 10$  per cent uncertainty on  $n_{\text{QSO}}$  due to the large-scale distribution of quasars: as in Outram et al. (2003), we typically find a  $\sim 10$  per cent difference in the number counts between the SGP and NGP. As this difference appears to be nearly constant as function of redshift, we quote for all subsamples the same typical uncertainty due to large scale structure. We note that our determination of  $n_{\text{QSO}}$  is independent of the normalisation constant  $\Phi^*$  appearing in equation (1).

From the luminosity function we also compute the effective redshift of the different samples as  $z_{\text{eff}} = \sum_{i=1}^{N_{\text{QSO}}} w_i z_i / \sum_{i=1}^{N_{\text{QSO}}} w_i$  (see Table 1).

### 2.3 Quasar projected correlation function

The simplest statistic which can be used to quantify clustering in the observed quasar distribution is the 2-point correlation function in redshift space,  $\xi^{\text{obs}}(r_{\perp}, \pi)$ . This measures the excess probability over random to find a quasar pair separated by  $\pi$  along the line of sight and by  $r_{\perp}$  in the plane of the sky. These separations are generally derived from the redshift and the angular position of each source, so that the inferred  $\pi$  includes a contribution from peculiar velocities. In consequence, the reconstructed clustering pattern in comoving space comes out to be a distorted representation of the real one and  $\xi^{\text{obs}}(r_{\perp}, \pi)$  is found to be anisotropic. To avoid this effect, and determine the quasar clustering amplitude in real space, one can then use the ‘‘projected correlation function’’ which is obtained by integrating  $\xi^{\text{obs}}(r_{\perp}, \pi)$  in the  $\pi$  direction:

$$\frac{\Xi^{\text{obs}}(r_{\perp})}{r_{\perp}} = \frac{2}{r_{\perp}} \int_0^{\infty} \xi^{\text{obs}}(r_{\perp}, \pi) d\pi, \quad (5)$$

and it is therefore unaffected by redshift-space distortions. In this section, we measure this quantity for our quasar samples.

We start by building a catalogue of unclustered points which has the same angular and radial selection function as the data. The angular selection is trivially given by the different completeness masks (see Croom et al. 2004 for further details), and we modulate the number of random points laid

down as a function of spectroscopic and photometric completeness. The radial selection function is instead obtained by heavily smoothing the observed quasar redshift distribution,  $\mathcal{N}(z)$ , or even the observed quasar comoving distance distribution,  $\mathcal{N}(r)$ . Both uniform and Gaussian smoothings, with characteristic smoothing length of several hundreds of  $h^{-1}$  Mpc, have been used. The quoted results are insensitive to the precise details of the modelling of the radial selection function. This is partially due to the fact that the volume covered by the quasar sample is very large and that there are not many clear groups or clusters of quasars: the quasar redshift distribution is rather smooth when compared to a standard galaxy distribution (e.g. Fig. 1 of Outram et al. 2003 vs Fig. 13 of Norberg et al. 2002b). As mentioned earlier, we do not apply any  $J_3$ -type weighting. In fact, the mean density of quasars,  $n_{\text{QSO}}$ , is so low that  $1 + 4\pi J_3 n_{\text{QSO}} \simeq 1$  for any reasonable quasar clustering amplitude.

The quasar correlation function is then estimated by comparing the probability distribution of quasar and random pairs on a two-dimensional grid of separations  $(r_{\perp}, \pi)$ . We use both the Landy-Szalay estimator (Landy & Szalay 1993) and the Hamilton estimator (Hamilton 1993):

$$\xi_{\text{LS}}^{\text{obs}} = \frac{DD - 2DR + RR}{RR}, \quad \xi_{\text{H}}^{\text{obs}} = \frac{DD \cdot RR}{(DR)^2} - 1 \quad (6)$$

where  $DD$ ,  $DR$  and  $RR$  are the suitably normalised numbers of weighted data-data, data-random and random-random pairs in each bin. We find, as expected, that the two estimators give comparable answers within the errors. For this reason, in what follows we only present results obtained with the Hamilton estimator.

Eventually, we compute the projected correlation function using equation (5). In order to avoid the measured signal to be dominated by noise, we limit the integration to an upper limit of  $\pi_{\text{max}} = 45 h^{-1}$  Mpc. Indeed, for line-of-sight separations larger than  $\pi_{\text{max}}$ , the number of quasar pairs with small transverse separations becomes very small. This is partially due to the sparseness of the samples considered, but also to the rareness of large structures of quasars. Therefore, with the current quasar sample, a reliable measure of  $\xi^{\text{obs}}(r_{\perp}, \pi)$  is not achievable on scales larger than  $\pi = 45 h^{-1}$  Mpc. Our results are not sensitive to the precise value adopted for  $\pi_{\text{max}}$ , but this limiting value needs to be sufficiently large in order to give a reliable and meaningful measurement of  $\Xi^{\text{obs}}(r_{\perp})/r_{\perp}$  on the scales of interest (i.e.  $r_{\perp} \lesssim 20 h^{-1}$  Mpc), but also small enough to be less sensitive to noise.

### 2.4 Error estimates for clustering measurements

It is common practice to estimate errors on the clustering measurements from mock surveys based on galaxy formation models. However, for quasars, such catalogues are not publicly available. We therefore opt for a bootstrap resampling technique. For each redshift-interval we divide both the NGP and the SGP samples into eight equal-volume regions, and we measure the clustering properties of each sub-sample. For ease of calculation, the division is just based on redshift and is such that the depth of each region is larger than the previously considered value for  $\pi_{\text{max}}$ . Since the number density is roughly constant as function of redshift, each of these regions approximately contains the same number of quasars.

<sup>2</sup> If the errors for the four parameters are statistically independent, the quoted values for  $\Delta n_{\text{QSO}}$  approximately give  $1\sigma$  uncertainties, whereas, if the parameters are correlated (which they most certainly are), the quoted errors for  $n_{\text{QSO}}$  correspond to a higher confidence interval.

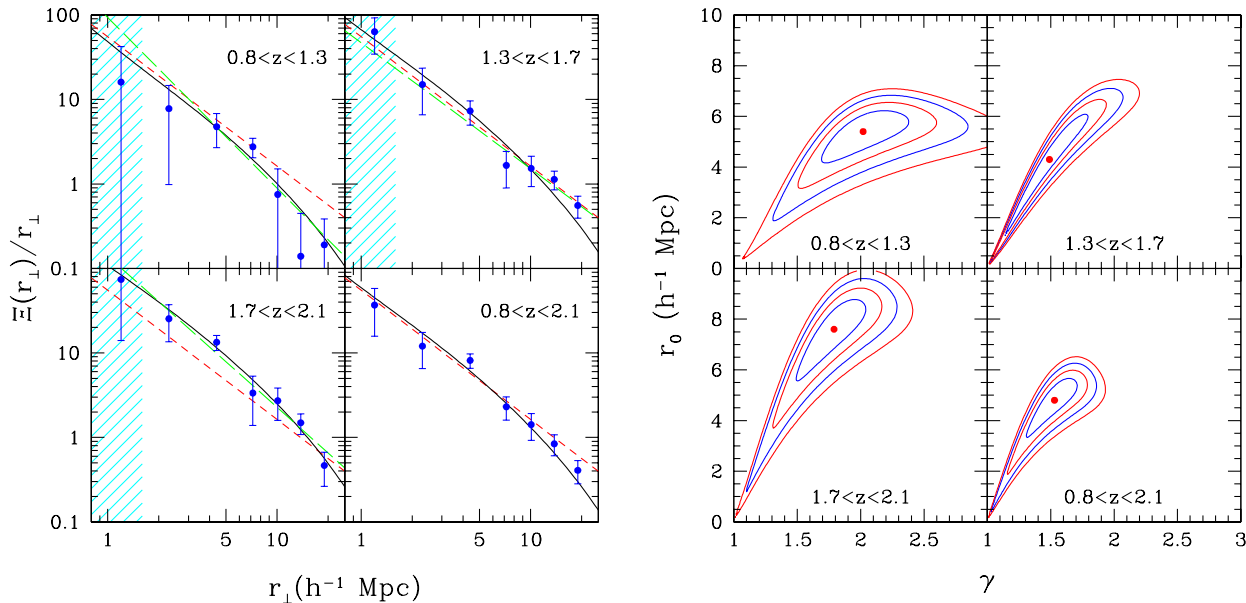


**Figure 1.** *Left panel:* The projected correlation function for different samples of quasars from the 2QZ (data with errorbars). For each redshift sub-sample, the best-fitting power law is represented with a long-dashed line. For reference, the best-fitting power law for the full sample ( $0.8 < z < 2.1$ ) is shown with a short-dashed line. The continuous lines represent the best-fitting constant-bias models discussed in Section 2.7. These functions practically coincide with the best-fitting halo-occupation models presented in Sections 3.3 and 5. Data in the shaded regions are derived from less than 20 quasar pairs and are not considered for model fitting. *Right panel:* Contour levels for the likelihood function obtained by fitting the data with a power law model. The best-fitting models are marked with a dot and the lines correspond to 4 different values of  $\Delta\chi^2 = \chi^2 - \chi_{\min}^2$ . In particular, for Gaussian errors, the inner contours ( $\Delta\chi^2 = 1$  and 2.3) mark the 68.3 per cent confidence levels for one and two parameters, respectively. Similarly, the outer contours ( $\Delta\chi^2 = 4$  and 6.17) correspond to the 95.4 per cent confidence levels for one and two parameters.

We then build 1000 bootstrap-samples, each of them composed by sixteen sub-samples (eight for each strip) randomly drawn (allowing repetitions) from the set described above. We measure the projected correlation function for each artificial sample by appropriately averaging over the number of quasar and random pairs of the sub-samples (and not over individual quasar clustering measurements). For each  $r_{\perp}$ , we identify the rms variation of  $\Xi$  over the bootstrap-samples with the  $1\sigma$  error for the projected correlation function.

Our method for estimating errors relies on the fact that our dataset is statistically representative of the quasar distribution in the Universe. However, this cannot be true for bins of spatial separations which contain just a few quasar pairs. Therefore, in what follows, we ignore clustering results obtained by less than 20 quasar pairs. Depending on the sample, this corresponds to  $r_{\perp} < 1 - 2 h^{-1}$  Mpc. Note that, on such scales, corrections for close pair incompleteness due to fibre collisions (Croom et al. 2004) should be also taken into account.

## 2.5 Results

The projected correlation function we obtained for the different redshift bins (and for the total sample) is presented in the left panel of Fig. 1. A clear evolutionary trend emerges from the data: the clustering amplitude for the high-redshift sample is nearly a factor of 2 (3) higher than for the total sample (low-redshift one).

As a zero-th order approximation, we fit our results with a power-law functional form. This phenomenological

description has been commonly used in the literature and allows us to compare our results with previous studies. More detailed modelling is presented in the next sections. Here, we assume that the quasar 2-point correlation function scales as

$$\xi(r) = \left(\frac{r_0}{r}\right)^{\gamma} \quad (7)$$

where  $r$  denotes the comoving separation between quasar pairs. The corresponding projected correlation function is obtained through the simple integral relation,

$$\Xi(r_{\perp}) = 2 \int_{r_{\perp}}^{\infty} \frac{r \xi(r)}{(r^2 - r_{\perp}^2)^{1/2}} dr, \quad (8)$$

which, in the power-law case, reduces to

$$\frac{\Xi(r_{\perp})}{r_{\perp}} = \frac{\Gamma(1/2) \Gamma[(\gamma - 1)/2]}{\Gamma(\gamma/2)} \left(\frac{r_0}{r_{\perp}}\right)^{\gamma} \quad (9)$$

with  $\Gamma(x)$  the Euler's Gamma function. We use a minimum least-squares method (corresponding to a maximum likelihood method in the case of Gaussian errors) to determine the values of  $r_0$  and  $\gamma$  that best describe the clustering data. A principal component analysis (see e.g. Porciani & Gialalisco 2002) is used here to deal with correlated errorbars. The principal components of the errors have been computed by diagonalizing the covariance matrix obtained by resampling the data with the bootstrap method described in the previous section. The objective function (the usual  $\chi^2$  statistic) has been obtained by considering the first four principal components which, for each redshift interval, account for more than 85 per cent of the variance.

**Table 2.** Best-fitting power law and constant-bias models for the four quasar samples. The goodness of each fit is measured by the quantity  $\chi^2_{\min}/\text{dof}$  which gives the minimum value assumed by the chi-square statistic divided by the number of degrees of freedom.

$z_{\min}$	$z_{\max}$	$r_0$ ( $h^{-1}$ Mpc)	$\gamma$	$\frac{\chi^2_{\min}}{\text{dof}}$	$r_0^{(\gamma=1.53)}$ ( $h^{-1}$ Mpc)	$\frac{\chi^2_{\min}}{\text{dof}}$	$r_0^{(\gamma=1.8)}$ ( $h^{-1}$ Mpc)	$\frac{\chi^2_{\min}}{\text{dof}}$	$b$	$\frac{\chi^2_{\min}}{\text{dof}}$
0.8	1.3	$5.4^{+0.9}_{-1.3}$	$2.02^{+0.36}_{-0.33}$	2.36/2	$3.4^{+0.6}_{-0.7}$	4.52/3	$4.7^{+0.7}_{-0.7}$	2.85/3	$1.80^{+0.20}_{-0.24}$	1.96/3
1.3	1.7	$4.3^{+1.8}_{-2.0}$	$1.49^{+0.32}_{-0.35}$	1.25/2	$4.6^{+0.4}_{-0.5}$	1.27/3	$6.0^{+0.4}_{-0.5}$	2.20/3	$2.62^{+0.18}_{-0.19}$	3.18/3
1.7	2.1	$7.6^{+1.2}_{-2.1}$	$1.79^{+0.25}_{-0.29}$	2.04/2	$5.9^{+0.7}_{-0.7}$	2.85/3	$7.6^{+0.8}_{-0.8}$	2.04/3	$3.86^{+0.32}_{-0.35}$	0.84/3
0.8	2.1	$4.8^{+0.9}_{-1.5}$	$1.53^{+0.19}_{-0.21}$	0.13/2	$4.8^{+0.6}_{-0.6}$	0.13/3	$5.4^{+0.5}_{-0.5}$	2.54/3	$2.42^{+0.20}_{-0.21}$	0.57/3

The best-fitting values for  $\gamma$  and  $r_0$  are given in Table 2 and the corresponding projected correlation functions are overplotted to the data in the left panel of Fig. 1. Contour plots of the  $\chi^2$  functions are shown in the right panel of Fig. 1. Note that the correlation length,  $r_0$ , and the slope of the correlation function,  $\gamma$ , are strongly covariant: in order to accurately describe the data, larger values of  $r_0$  need to be associated with steeper slopes. The best-fitting slope for the whole quasar sample,  $\gamma = 1.53^{+0.19}_{-0.21}$ , is in very good agreement with the redshift-space analysis by Croom et al. (2001) who found  $\gamma = 1.56^{+0.10}_{-0.09}$  at a mean redshift of  $\bar{z} = 1.49$ . This is not surprising, since we only consider scales that are in the quasi-linear and linear regime of gravitational instability where the correlation function in real and redshift-space are proportional to each other (Kaiser 1987). Accordingly, the comoving correlation length we find in real space,  $r_0 = 4.8^{+0.9}_{-1.5} h^{-1}$  Mpc, is, as expected, slightly smaller than its redshift-space counterpart,  $5.69^{+0.42}_{-0.50} h^{-1}$  Mpc.<sup>3</sup>

As previously discussed, visual inspection of Fig. 1 suggests that the quasar clustering amplitude at  $1.7 < z < 2.1$  is nearly a factor of 2 higher than that obtained for the whole sample. Two sigma evidence for an increase in the clustering amplitude of optically selected quasar between  $z \sim 1$  and  $z \sim 1.8$  has been presented by La Franca, Andreani & Cristiani (1998). However, given their sample size (a few hundred quasars) it is not clear whether the detected evolution is real or it is spuriously created by cosmic variance effects (see e.g. the discussion in Croom et al. 2001 who, using a preliminary data release of the 2QZ, found a that the redshift-space clustering amplitude at  $z = 2.7$  is a factor 1.4 higher than at  $z = 0.7$  which is marginally significant). It is therefore interesting to try to quantify the evolution of the clustering amplitude in our large quasar sample. In order to facilitate the comparison among the different subsamples (and with previous studies), we report in Table 2 the 68.3 per cent confidence intervals for  $r_0$  obtained by assuming  $\gamma = 1.53$  ( $r_0^{(\gamma=1.53)}$ ) and  $\gamma = 1.80$  ( $r_0^{(\gamma=1.80)}$ ). When fixing the slope, we note a steady increase of the quasar correlation length with  $z$ . Within this approximation, clustering evolution with redshift is detected at the  $\sim 3.6\sigma$  confidence level. However, since we are dealing with a flux-limited sample (where the highest-redshift objects have on average the highest intrinsic

luminosities), it is not possible to say whether this evolution of  $r_0$  corresponds to a real change in the quasar population or to clustering segregation with luminosity. By analysing quasar clustering in the range  $0.3 < z < 2.9$  as a function of apparent luminosity in the preliminary data release catalogue of the 2QZ, Croom et al. (2002) found weak ( $\simeq 1\sigma$ ) evidence for the brightest third of quasars on the sky to be more clustered than the full data set. Even though the different selection criteria prevent a direct comparison, we find a statistically more significant change in the clustering strength among our sub-samples than that reported in Croom et al. (2002). We defer a detailed analysis of the luminosity dependence of quasar clustering to future work.

## 2.6 QSO vs galaxy clustering

How do our results on the spatial distribution of quasars compare with galaxy clustering at similar redshifts? Until very recently, only rather small samples of high-redshift galaxies were available and any attempt to determine their clustering properties was most probably hampered by cosmic variance (e.g. Le Fèvre et al. 1996; Carlberg et al. 1997; Arnouts et al. 1999; Magliocchetti & Maddox 1999). The advent of color-selected surveys has allowed the detection of rich and homogeneous samples of high-redshift galaxies over relatively large volumes. We want to compare the results obtained from the largest samples presently available with those obtained from our sample of quasars. A number of studies have shown that Lyman-break galaxies at  $z \sim 3$  are strongly clustered (e.g. Porciani & Giavalisco 2002 and references therein). Both their correlation length,  $r_0 \sim 4 h^{-1}$  Mpc, and the slope of  $\xi$ ,  $\gamma \sim 1.5$ , (Porciani & Giavalisco 2002; Adelberger et al. 2003) are remarkably similar to the values obtained from our quasar sample. On the other hand, star-forming galaxies at  $z \simeq 1$  (detected by exploiting the Balmer break in their spectra) are found to be slightly less clustered:  $r_0 \sim 3 h^{-1}$  Mpc with  $\gamma \sim 1.7$  (Adelberger 2000). Similarly, the galaxy-galaxy correlation function from the DEEP2 Galaxy Redshift Survey at  $z_{\text{eff}} = 1.14$  is well described by a power law with  $\gamma = 1.66 \pm 0.12$  and  $r_0 = 3.1 \pm 0.7 h^{-1}$  Mpc (Coil et al. 2004). Evidence that early-type galaxies are more clustered than late-type ones (Firth et al. 2002; Coil et al. 2004) might help reconciling these results with those inferred from the quasar population. Extremely red galaxies at  $z \sim 1$  have been found to be exceptionally strongly clustered. Assuming  $\gamma = 1.8$  (as inferred from their angular clustering) one finds  $r_0 \sim 12$

<sup>3</sup> Croom et al. (2001) assume statistically independent Poisson errorbars for the correlation function at different separations. This explains the factor of 2 between their and our estimate of the uncertainty for  $r_0$  and  $\gamma$ .

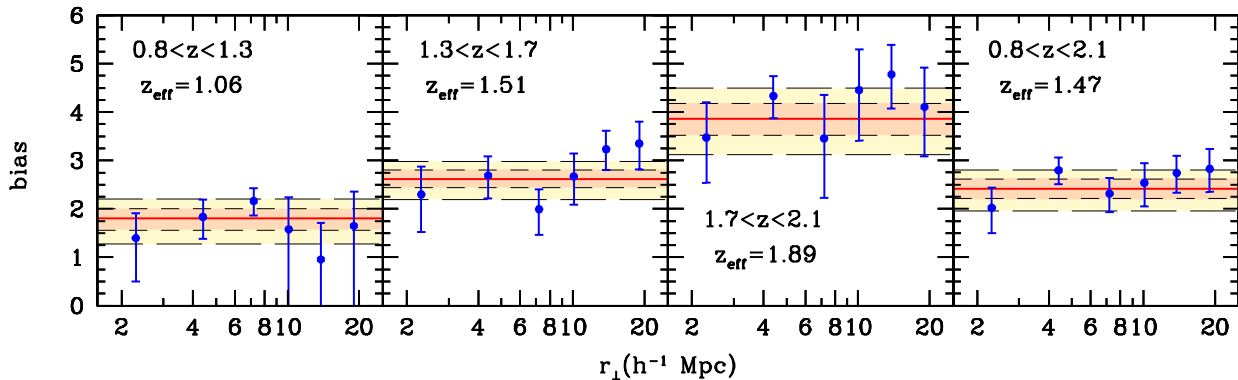


**Figure 2.** Quasar-to-mass bias function derived by applying equation (10) to quasar samples within different redshift ranges (points with errorbars). The continuous line shows the best fitting constant value. Shaded regions indicate the values of the bias for which  $\Delta\chi^2 < 1$  (dark shading) and  $\Delta\chi^2 < 4$  (light shading).

$h^{-1}$  Mpc (Daddi et al. 2001; Firth et al. 2002; Roche, Dunlop & Almaini 2003).

## 2.7 QSO vs dark-matter clustering

To study how the spatial distribution of quasars relate to the underlying matter distribution, we introduce the quasar-to-mass bias function:

$$b(r_{\perp}, z_{\text{eff}}) = \left[ \frac{\Xi(r_{\perp}, z_{\text{min}} < z < z_{\text{max}})}{\Xi_{\text{m}}(r_{\perp}, z_{\text{eff}})} \right]^{1/2} \quad (10)$$

where  $\Xi_{\text{m}}$  is the projected correlation function of the mass distribution in the assumed cosmology computed as in Peacock & Dodds (1996). Fig. 2 shows our results for the different redshift bins. Errorbars at different spatial separations are not statistically independent. As previously described, we fit the data with a constant function by using the principal components of the bootstrap errors (which shows that datapoints at  $r_{\perp} > 10 h^{-1}$  Mpc are strongly correlated). Results and the corresponding  $1\sigma$  uncertainties are listed in Table 2.

We find that  $b$  steadily increases with  $z$ . This statistically significant trend is mostly due to the rapid evolution of the mass autocorrelation function.

## 3 THE HALO OCCUPATION NUMBER OF QUASARS

In this section, we present the halo model for the spatial distribution of quasars. After introducing the basic notation, we describe the main features which characterize our model.<sup>4</sup> We then use the number density and the projected correlation function determined in Section 2 to constrain the free parameters of the halo model. This allows us to

<sup>4</sup> Further details can be found in Magliocchetti & Porciani (2003) where we used a similar tool to study the clustering properties of galaxies with different spectral types in the 2dF Galaxy Redshift Survey (2dFGRS).

determine the way quasars populate dark-matter haloes of different masses.

### 3.1 The halo model

It is generally believed that quasars are powered by mass accretion onto supermassive black holes lying at the centre of galaxies. Cold dark matter (CDM) models for structure formation predict that galaxies form within extended dark-matter haloes. The number density and clustering properties of these haloes can be easily computed, at any redshift, by means of a set of analytical tools which have been tested and calibrated against numerical simulations (e.g. Mo & White 1996; Sheth & Tormen 1999). In consequence, the problem of discussing the abundance and spatial distribution of quasars can be reduced to studying how they populate their host haloes. The basic quantity here is the halo occupation distribution function,  $P_N(M)$ , which gives the probability of finding  $N$  quasars within a single halo as a function of the halo mass,  $M$ . Given the halo mass function  $n(M)$  (number of dark-matter haloes per unit mass and volume), the mean value of the halo occupation distribution  $N(M) = \langle N \rangle(M) = \sum_N N P_N(M)$  (which from now on will be referred to as the halo occupation number) completely determines the mean comoving number density of quasars:

$$\bar{n} = \int n(M) N(M) dM. \quad (11)$$

Analogous relations, involving higher-order moments of  $P_N(M)$ , can be used to derive the clustering properties of quasars in the halo model. For instance, the 2-point correlation function can be written as the sum of two terms

$$\xi(r) = \xi^{1h}(r) + \xi^{2h}(r). \quad (12)$$

The function  $\xi^{1h}$ , which accounts for pairs of quasars residing within the same halo, depends on the second factorial moment of the halo occupation distribution,  $\Sigma^2(M) = \langle N(N-1) \rangle(M)$  and on the spatial distribution of quasars

within their host haloes,  $\rho(\mathbf{x}; M)$ ,<sup>5</sup>

$$\xi^{\text{1h}}(r) = \int \frac{n(M) \Sigma^2(M)}{\bar{n}^2} dM \int \rho(\mathbf{x}; M) \rho(\mathbf{x} + \mathbf{r}; M) d^3x. \quad (13)$$

On the other hand, the contribution to the correlation coming from quasars in different haloes,  $\xi_{\text{QSO}}^{\text{2h}}$ , depends on  $N(M)$  and  $\rho(\mathbf{x}; M)$  as follows

$$\xi^{\text{2h}}(r) = \int \frac{n(M_1) N(M_1)}{\bar{n}} dM_1 \int \frac{n(M_2) N(M_2)}{\bar{n}} dM_2 \times \int \rho(\mathbf{x}_1; M_1) \rho(\mathbf{x}_2; M_2) \xi_{\text{h}}(\mathbf{r}_{12}; M_1, M_2) d^3r_1 d^3r_2, \quad (14)$$

where  $\mathbf{r}_i$  marks the position of the centre of each halo,  $\mathbf{r}_{12} = \mathbf{r}_2 - \mathbf{r}_1$  is the separation between the haloes,  $\mathbf{x}_i$  denotes the quasar position with respect to each halo centre (hence  $\mathbf{r} = \mathbf{r}_{12} + \mathbf{x}_2 - \mathbf{x}_1$ ), and  $\xi_{\text{h}}(r_{12}; M_1, M_2)$  is the cross-correlation function of haloes of mass  $M_1$  and  $M_2$ , separated by  $r_{12}$ . For separations which are larger than the virial radius of the typical quasar-host halo, the 2-halo term dominates the correlation function. In this regime,  $\xi_{\text{h}}(r; M_1, M_2)$  scales proportionally to the mass autocorrelation function,  $\xi_{\text{m}}(r)$ , as  $\xi_{\text{h}}(r; M_1, M_2) \simeq b(M_1) b(M_2) \xi_{\text{m}}(r)$ , with  $b(M)$  the linear-bias factor of haloes of mass  $M$  (Cole & Kaiser 1989; Mo & White 1996; Catelan et al. 1997; Porciani et al. 1998). As a consequence of this, the large-scale behaviour of the quasar correlation function also comes out to be  $\xi(r) \simeq b_{\text{eff}}^2 \xi_{\text{m}}(r)$ , with

$$b_{\text{eff}} = \frac{\int b(M) N(M) n(M) dM}{\int N(M) n(M) dM}. \quad (15)$$

Note that all the different quantities introduced in this section depend on the redshift  $z$ , even though we have not made it explicit in the equations.

In order to use the halo model to study quasar clustering, one has to specify a number of functions describing the statistical properties of the population of dark-matter haloes. In general, these have either been obtained analytically and then calibrated against N-body simulations, or directly extracted from numerical experiments. For the mass function and the linear bias factor of dark-matter haloes we adopt here the model by Sheth & Tormen (1999). We approximate the 2-point correlation function of dark-matter haloes with the function (see e.g. Porciani & Giallisco 2002; Magliocchetti & Porciani 2003)

$$\xi_{\text{h}}(r; M_1, M_2) = \begin{cases} b(M_1) b(M_2) \xi_{\text{m}}(r) & \text{if } r \geq r_1 + r_2 \\ -1 & \text{if } r < r_1 + r_2 \end{cases} \quad (16)$$

where the mass autocorrelation function,  $\xi_{\text{m}}(r)$ , is computed using the method introduced by Peacock & Dodds (1996) which, for our purposes, is sufficiently accurate both in the linear and non-linear regimes.<sup>6</sup> For small separations, equation (16) accounts for spatial exclusion between haloes (e.g. 2 haloes cannot occupy the same volume). In Section 5.4,

<sup>5</sup> This is normalised in such a way that  $\int_0^{r_{\text{vir}}} \rho(\mathbf{y}; M) d^3y = 1$  where  $r_{\text{vir}}$  is the virial radius which is assumed to mark the outer boundary of the halo.

<sup>6</sup> In principle, for separations where  $\xi_{\text{m}}(r) \sim 1$ , non-linear terms should be added to equation (16) (Mo & White 1996; Catelan et al. 1997; Porciani et al. 1998). However, for the haloes and redshifts of interest, these can be safely neglected.

where we discuss the small-scale clustering of quasars, we identify the Eulerian zone of exclusion of a given halo,  $r_i$ , with its virial radius. At the same time, we assume that quasars trace the dark-matter distribution and adopt, for  $\rho(\mathbf{x}; M)$  a Navarro, Frenk & White (1997; NFW) profile with concentration parameter obtained from equations (9) and (13) of Bullock et al. (2001). Note that, in all the other sections of this paper, we only consider the large scale distribution of quasars ( $r \gtrsim 2 h^{-1}$  Mpc), where exclusion effects and density profiles do not affect the predictions of the halo model for  $\xi$ .

### 3.2 Clustering on the light-cone

Equations (12), (13) and (14) describe the clustering properties of a population of cosmic objects selected in a three-dimensional spatial section taken at constant cosmic time in the synchronous gauge. However, deep surveys like the 2QZ span a wide interval of lookback times and the equations we have introduced above do not apply in this case.

A number of authors have discussed 2-point statistics of objects lying on the light-cone of the observer (e.g. Matarrese et al. 1997, Yamamoto & Suto 1999, Moscardini et al. 2000 and references therein). These works have shown that the observed correlation function can be written as the weighted average:

$$\xi^{\text{obs}}(r) = \frac{\int_{z_{\text{min}}}^{z_{\text{max}}} \mathcal{W}(z) \xi(r, z) dz}{\int_{z_{\text{min}}}^{z_{\text{max}}} \mathcal{W}(z) dz}, \quad (17)$$

where  $\mathcal{W}(z) = \mathcal{N}(z)^2 (dV/dz)^{-1}$ , with  $\mathcal{N}(z)$  the actual redshift distribution of the objects in the sample and  $dV/dz$  the Jacobian between comoving volume and redshift. Note that equation (17) only holds for scales  $r$  over which: *i*)  $\mathcal{N}$  is nearly constant and *ii*)  $\xi$  does not significantly evolve over the time  $r/[(1+z)c]$  (where  $c$  denotes the speed of light in vacuum). Within the range of separations covered by our dataset, both the conditions are satisfied for our quasar sample.

Combining equations (8), (12) and (17), we compute  $\Xi^{\text{obs}}(r_{\perp})$  in our 4 redshift intervals for a large set of  $N(M)$  models and then compare the results with  $\Xi(r_{\perp}, z_{\text{eff}})$ , the constant-time correlation function evaluated by using equations (8) and (12) at the effective redshift of each subsample. In all cases we find extremely good agreement between the two functions. Even for the widest redshift bin,  $0.8 < z < 2.1$ , we find a maximum discrepancy of 2 per cent which is negligibly small with respect to the typical error associated with the observed correlation function. Therefore, in what follows, we use  $\Xi(r_{\perp}, z_{\text{eff}})$  to compare the predictions of different models with the clustering data. This greatly simplifies (and speeds-up) the model fitting procedure. As an additional test, the comparison between  $\Xi^{\text{obs}}(r_{\perp})$  and  $\Xi(r_{\perp}, z_{\text{eff}})$  is repeated for all the best-fitting models that are discussed in the forthcoming sections and no significant difference is found.

### 3.3 The halo occupation number

The final, key ingredient needed to describe the clustering properties of quasars is their halo occupation distribution



function. In the most general case,  $P_N(M)$  is entirely specified by all its moments which, in principle, could be observationally determined by studying quasar clustering at any order. Regrettably, as we have already shown in Section 2.5, quasars are so rare that their 2-point function is already very poorly determined so that it is not possible to accurately measure higher-order statistics. As in Magliocchetti & Porciani (2003), we overcome this problem by assuming a predefined functional form for the lowest-order moments of  $P_N(M)$ . It is, in fact, convenient to describe the halo occupation number,  $N(M)$ , and (if necessary) its associated scatter,  $\Sigma^2(M)$ , in terms of a few parameters whose values will then be constrained by the data.

### 3.3.1 A set of simple models for $N(M)$

In Section 2.7 we showed that quasar clustering is consistent with the assumption of a constant bias parameter as a function of spatial separation. Therefore, combining the clustering information with the quasar number density we can fully constrain  $N(M)$  models containing two free parameters. We consider here three different options:

$$N(M) = N_L \cdot \exp \left[ -8 \left( \log_{10} \frac{M}{M_L} \right)^2 \right]; \quad (18)$$

$$N(M) = N_T \cdot \Theta \left( \frac{M}{M_T} - 1 \right); \quad (19)$$

$$N(M) = N_E \cdot \Theta \left( \frac{M}{M_E} - 1 \right) \cdot \frac{M}{M_E}; \quad (20)$$

where  $\Theta(x)$  denotes the Heavyside probability distribution function. Equation (18) assumes that quasar-host haloes have a characteristic mass  $M_L$ . The halo occupation number peaks at  $M_L$  and it is reduced by a factor  $f > 1$  with respect to its maximum value for  $M = 10^{\pm[(\ln f)/8]^{1/2}} M_L$ . This corresponds to  $M = 10^{\pm 0.54} M_L$  for  $f = 10$ , and to  $M = 10^{\pm 0.76} M_L$  for  $f = 100$ . In other words, the allowed variation of the halo mass spans a factor of  $\sim 10$ . Equations (19) and (20), instead, allow for a wide mass spectrum for quasar-hosts. The basic assumption, in this case, is that only haloes whose mass is above a given threshold will be able to host the bright quasars detected in the 2QZ survey. In equation (19), the mean number of quasars per halo is  $N_T$  for all haloes with  $M > M_T$ . This functional form has been used by Croom et al. (2001) to discuss the clustering of 2QZ quasars in redshift-space. Finally, equation (20) assumes that the number of quasars hosted by a single halo is directly proportional to the halo mass. This model has been inspired by our analysis of the clustering of early-type galaxies in the 2dFGRS where, for large halo masses, the halo occupation number scales almost linearly with  $M$  (Magliocchetti & Porciani 2003). Note that the free parameters of the models (18), (19) and (20) can be naturally split into two groups. On the one hand,  $M_L$ ,  $M_T$  and  $M_E$  determine which kind of haloes host the quasars. On the other hand,  $N_L$ ,  $N_T$  and  $N_E$  indicate how many quasars are on average hosted by each halo.

In the range of separations covered by our dataset ( $r \gtrsim 2 h^{-1}$  Mpc), the two-halo term dominates the amplitude of the quasar 2-point correlation function and there is no need to specify the form of the function  $\Sigma^2(M)$ .

It is important to stress here that any observational result on the number density of quasars will give degenerate constraints on the parameters of the models. In fact, one can obtain the same density of quasars either by considering abundant, small mass haloes which are scarcely populated, or by taking into account rare, massive haloes containing numerous quasars. However, clustering data can break this degeneracy, since the quasar correlation function on large scales does not depend on the overall normalisation of  $N(M)$  (see equation 15).

### 3.3.2 Best-fitting models

We use a minimum least-squares method to determine the values of the parameters which best describe the observational datasets. As discussed in Section 2.5, we use a principal component analysis of the errors to deal with the clustering data. For each model, we then build a “total” likelihood function

$$\mathcal{L}_{\text{tot}}(M_i, N_i) = \mathcal{L}_{\text{clust}}(M_i) \cdot \mathcal{L}_{\text{dens}}(M_i, N_i) \quad (21)$$

where  $\mathcal{L}_{\text{clust}}$  accounts for the large-scale clustering analysis presented in Section 2.5 and  $\mathcal{L}_{\text{dens}}$  for the quasar number density.<sup>7</sup> In other words, the number density constraints weights as much as a single independent point in the clustering analysis. Note that this analysis improves upon our previous work (Magliocchetti & Porciani 2003), where we considered a top-hat  $\mathcal{L}_{\text{dens}}$  which assumes a constant value when  $\bar{n}$  lies within  $2\sigma$  from the observed value, and vanishes otherwise. Beyond presenting a sharp edge, the function adopted in Magliocchetti & Porciani (2003) has the additional drawback of giving the same weight to all the allowed values, without favouring those close to the observed one.

The resulting  $1\sigma$  intervals for the single parameters in models (18), (19) and (20) are reported in Table 3. In general, we find that  $M_i \sim 10^{12-13} M_\odot$  and  $N_i \sim 10^{-2-3}$ . Since model E gives more weight to larger halo masses, both  $M_E$  and  $N_E$  tend to be smaller than in the other cases. Clear evolutionary trends are present in the results. For each model, both  $M_i$  and  $N_i$  tend to increase with redshift. This might suggest that brighter quasars are hosted by more massive haloes. Note that, in all cases, the mean mass of a quasar host lies in the narrow range between  $6 \times 10^{12} M_\odot$  and  $2 \times 10^{13} M_\odot$  and shows a mild increment with the effective redshift of the chosen sub-sample. This model-independent statement clearly is the most important result of this analysis.

### 3.3.3 Estimating the quasar lifetime

The number of optically bright quasars per halo can be used to estimate the duty cycle of quasar activity and, thus, the quasar lifetime (Haiman & Hui 2001; Martini & Weinberg 2001). In brief, let us assume, for simplicity, that each dark-matter halo contains one supermassive black-hole. In this case, the fraction of active quasars per halo coincides with the quasar duty cycle. Assuming that quasar activity is

<sup>7</sup> Assuming Gaussian errors,  $-2 \ln \mathcal{L}_i = \chi_i^2 + \text{const}$  where  $\chi_i^2$  denotes the usual chi-square statistic.

**Table 3.** Best-fitting parameters for the halo-occupation models discussed in Section 3.3.1. The symbols  $\langle M \rangle$  and  $t_Q$  denote, respectively, the mean mass of the haloes which are hosting quasars in the relevant redshift range and the quasar lifetime.

$z_{\min}$	$z_{\max}$	model	$\log_{10} \frac{M_i}{M_\odot}$	$\log_{10} N_i$	$\frac{\chi^2_{\min}}{\text{dof}}$	$\log_{10} \frac{\langle M \rangle}{M_\odot}$	$\log_{10} N(\langle M \rangle)$	$\frac{t_Q}{10^7 \text{yr}}$
0.8	1.3	L	$12.9^{+0.1}_{-0.3}$	$-2.1^{+0.3}_{-0.3}$	1.96/2	12.81	-2.1	2.9
0.8	1.3	T	$12.4^{+0.2}_{-0.3}$	$-2.3^{+0.2}_{-0.4}$	1.96/2	12.91	-2.3	1.8
0.8	1.3	E	$11.2^{+0.5}_{-1.1}$	$-4.3^{+0.6}_{-1.3}$	1.96/2	13.20	-2.3	1.8
1.3	1.7	L	$13.2^{+0.1}_{-0.2}$	$-1.6^{+0.1}_{-0.2}$	3.18/2	13.04	-1.7	4.9
1.3	1.7	T	$12.7^{+0.1}_{-0.2}$	$-1.9^{+0.2}_{-0.2}$	3.18/2	13.07	-1.9	3.1
1.3	1.7	E	$12.2^{+0.2}_{-0.3}$	$-3.0^{+0.3}_{-0.4}$	3.18/2	13.20	-2.0	2.5
1.7	2.1	L	$13.5^{+0.1}_{-0.1}$	$-1.0^{+0.2}_{-0.3}$	0.84/2	13.30	-1.1	15
1.7	2.1	T	$13.0^{+0.2}_{-0.1}$	$-1.2^{+0.3}_{-0.2}$	0.84/2	13.28	-1.2	12
1.7	2.1	E	$12.8^{+0.1}_{-0.2}$	$-1.9^{+0.2}_{-0.3}$	0.84/2	13.34	-1.4	7.8
0.8	2.1	L	$13.1^{+0.1}_{-0.2}$	$-1.6^{+0.2}_{-0.2}$	0.57/2	12.95	-1.7	5.3
0.8	2.1	T	$12.6^{+0.1}_{-0.2}$	$-1.8^{+0.2}_{-0.3}$	0.57/2	13.00	-1.8	4.0
0.8	2.1	E	$12.0^{+0.2}_{-0.4}$	$-3.1^{+0.3}_{-0.5}$	0.57/2	13.15	-2.0	2.6

randomly triggered (for instance by tidal interactions with neighbours) during the halo lifetime,  $t_H$ , the duty cycle can then be expressed as  $t_Q/t_H$  where  $t_Q$  denotes a characteristic timescale over which the quasar is visible in the optical band. Both a single optically bright phase and a series of shorter bursts can correspond to the same  $t_Q$ . We use here the halo occupation number evaluated at the mean host-halo mass,  $N(\langle M \rangle)$  to estimate the quasar duty cycle. This eliminates any mass dependence. Following Martini & Weinberg (2001), the halo lifetime is defined as the median time interval during which a halo of mass  $M$  at redshift  $z$  is incorporated into a halo of mass  $2M$ . This quantity is computed using equation (2.22) of Lacey & Cole (1993). Results for  $t_Q$  are listed in Table 3. Independently of the model for  $N(M)$ , we find that the quasar duty cycle and  $t_Q$  increase with  $z$ . For our sample at  $z_{\text{eff}} = 1.06$ , we find that only  $\sim 0.5$  per cent of the host-haloes contain a bright quasar, which corresponds to  $t_Q \simeq 2 \times 10^7$  yr. This coincides with the  $e$ -folding time of a black hole which accretes mass with a radiative efficiency  $\epsilon \sim 0.1$  and shines at a fraction  $\eta \sim 0.5$  of its Eddington luminosity (Salpeter 1964). On the other hand, at  $z_{\text{eff}} = 1.89$ , the fraction of active black-holes increases to 4-8 per cent and  $t_Q \simeq 10^8$  yr. Note that, given the simplicity of the model, our results are only indicative. The quoted quasar lifetimes should be revised upwards if: (i) a non-negligible number of haloes do not harbour any supermassive black-hole; (ii) optical radiation from quasars turns out to be significantly beamed; (iii) in the presence of an important fraction of obscured sources. On the other hand,  $t_Q$  is smaller than what reported here if more than one supermassive black-hole is hosted, on average, by each halo.

High-resolution optical imaging with the *Hubble Space Telescope* (HST) shows that bright quasars ( $M_V < -23$ ) at  $z < 0.5$  are only harboured by exceptionally luminous galaxies with  $L \gtrsim L_V^*$  (Bahcall et al. 1997; Hamilton, Caser-

tano & Turnshek 2002). These galaxies turn out to be a mixture of different morphological types, ranging from normal ellipticals and spirals to complex systems of gravitationally interacting components (Bahcall et al. 1997). However, a number of observational results suggest that spheroidal hosts become more prevalent with increasing nuclear luminosities: quasars with  $M_V < -23.5$  are virtually all harboured by luminous elliptical galaxies (Dunlop et al. 2003). Similarly, observed surface-brightness profiles suggest that bright quasars at  $z \sim 1 - 2$  are hosted by massive ellipticals undergoing passive evolution (Kukula et al. 2001; Falomo et al. 2004).<sup>8</sup> Taking this for granted, we can show that our assumption of one supermassive black hole per halo (and thus our inferred quasar lifetime) is rather realistic. The argument proceeds as follows. (i) Massive elliptical galaxies are made of old stellar populations which formed at  $z \gtrsim 2$  and passively evolved thereafter. (ii) In the assumed cosmology, the massive haloes which harbour these galaxies can only increase their mass by a factor of a few from  $z = 1 - 2$  to the present epoch. This mainly happens via accretion of smaller objects. (iii) From clustering studies in the local Universe, we derive that haloes with  $M \sim 10^{13-14} M_\odot$  harbour on average  $\sim 1 - 2$  early-type galaxies with effective luminosity  $L_{\text{eff}} = 1.3 L^*$  (Magliocchetti & Porciani 2003). Points (i), (ii) and (iii) imply that the mean number of early-type galaxies per halo was of order unity even at  $z \sim 1 - 2$ . Thus, our

<sup>8</sup> Other authors draw different conclusions. For instance, Hutchings et al. (2002) find that, even though the resolved flux of quasar hosts at  $z \sim 2$  can be fitted by a de Vaucouleurs profile, the corresponding optical images show asymmetries and rather irregular morphologies. A faint, disc-like component extending to large radii is always needed to accurately fit the data. This agrees with low-redshift observations in the near-infrared ( $K$ -band) showing that, in some cases, quasar hosts are dominated by a disc component on scales much larger than those probed in optical images (Percival et al. 2001).

this follows from the assumption that each galaxy hosts a single supermassive black hole.

Similar reasoning cannot be applied to the population of late-type galaxies which formed much more recently. Local star-forming galaxies with  $L > L^*$  are slightly less abundant than their late-type counterparts (Madgwick et al. 2002; see also Fig. 9 in Norberg et al. 2002a). However, their abundance at higher redshifts is loosely constrained by observations. Therefore, our estimates for  $t_Q$  might need substantial revision if a significant fraction of quasars is hosted by late-type galaxies.

#### 4 THE HALO OCCUPATION NUMBER FROM QUASAR LUMINOSITIES

Recent studies of stellar and gas dynamics in local galaxies have revealed a wealth of information on the population of supermassive black holes. The observed correlation between the mass of a black hole,  $M_{\text{bh}}$ , and the circular velocity,  $v_c$ , of its host galaxy (Ferrarese 2002; Baes et al. 2003) is one of the most intriguing results. In this section, we use this empirically determined relation ( $M_{\text{bh}} \propto v_c^{4.2}$ ) to derive the halo occupation number of quasars in the 2QZ. This is obtained by first converting quasar luminosities into a distribution of black-hole masses (to which we apply the  $M_{\text{bh}} - v_c$  correlation) and then linking, with minimal assumptions, the circular velocity of the host galaxies to the mass of their dark-matter halo. Eventually, we test whether the resulting halo occupation number is consistent with the quasar clustering data we measured in Section 2.5.

##### 4.1 Black-hole masses

The bolometric luminosity of a quasar and the mass of the accreting black hole can be related as follows

$$\frac{M_{\text{bh}}}{M_{\odot}} = \frac{1}{\eta} \frac{L_{\text{bol}}}{1.26 \times 10^{38} \text{ erg s}^{-1}} \quad (22)$$

where  $\eta$  denotes the ratio between the bolometric luminosity of the quasar and the Eddington luminosity. We want to use this relation to determine the typical black-hole mass associated with a quasar of a given blue luminosity. In order to do this, we use a number of observational results to estimate the bolometric luminosity of an object starting from its absolute magnitude in  $b_J$ , and to get the probability density function of  $\eta$ .

###### 4.1.1 From photographic to Johnson $B$ magnitudes

We start from converting  $b_J$  fluxes into standard  $B$  magnitudes. In general,  $B \simeq b_J + 0.3(B - V)$  (Blair & Gilmore 1982; Colless et al. 2001), and the rest-frame color index for quasars is  $B - V \simeq 0.22$  (Cristiani & Vio 1990). In what follows, we then assume

$$M_B = M_{b_J} + 0.07, \quad (23)$$

which is in good agreement with Brotherton et al. (2001). Note that the amplitude of the correction is comparable with the statistical error which affects the magnitude determination in the 2dFGRS (Colless et al. 2001; Norberg et al. 2002b) which uses the same UKST photographic plates as

the 2QZ. It is then reasonable to expect that also quasar photometry in the 2QZ is affected by typical errors of  $\sim 0.1$  magnitudes (e.g. Corbett et al. 2003).

###### 4.1.2 Bolometric corrections

In order to use equation (22) to infer the mass of the black holes which power 2QZ quasars, we need to convert their absolute  $B$  magnitudes into bolometric luminosities. Bolometric corrections for a sample of X-ray selected quasars lying at  $z < 1$  have been derived in a seminal paper by Elvis et al. (1994). Since observations show that quasar spectra do not evolve with  $z$  (e.g. Bechtold et al. 1994), it is common practice to apply these corrections also to high-redshift quasars. It has been recently pointed out, however, that the bolometric corrections by Elvis et al. (1994) are seriously affected by systematics and should be revised downwards (e.g. Fabian & Iwasawa 1999; Elvis, Risaliti & Zamorani 2002). For this reason we use here the results by McLure & Dunlop (2004) who, adopting the revised template spectrum by Elvis et al. (2002), estimated the bolometric corrections for 1136 quasars at  $0.5 < z < 0.8$  extracted from the SDSS. Corrections from the B band have then been computed using a subsample of 372 objects common to the 2dF and SDSS surveys. When combined with equation (23), their best fitting relation gives

$$\log_{10} \left( \frac{L_{\text{bol}}}{10^{46} \text{ erg s}^{-1}} \right) = 0.21 - 0.38 (M_{b_J} + 25) \quad (24)$$

and the corresponding rms variation at fixed  $M_{b_J}$  is 0.14. Within the quoted uncertainties, this is perfectly consistent with the recent results by Marconi et al. (2004).<sup>9</sup>

###### 4.1.3 The Eddington ratio and the distribution of black-hole masses

Observational estimates of the Eddington ratio,  $\eta$ , require: (i) using some dynamical tracer to determine the black-hole mass (and thus the Eddington luminosity); (ii) measuring the quasar luminosity in a given band,  $L_i$ ; (iii) applying the corresponding bolometric correction,  $\beta_i^{\text{bol}}$ ; (iv) calculating  $\eta \propto \beta_i^{\text{bol}} L_i / M_{\text{bh}}$ . Given this complexity, measurements of  $\eta$  are rather uncertain and sensitive to a number of sources of systematic errors. Recent determinations, however, tend to lie in the same ballpark and suggest that  $\eta$  mildly increases with  $z$  (Dunlop et al. 2003; McLure & Dunlop 2004). For consistency with section 4.1.2, we use here the results by McLure & Dunlop (2004) who combined virial estimates of black hole masses with new bolometric corrections to infer the Eddington ratio for a large sample of quasars from the SDSS. From their results we infer that, for  $0.8 < z < 2.1$ , the probability density function for  $\log_{10} \eta$  is well approximated by a Gaussian distribution with mean  $0.21z - 0.80$  and variance  $\sim 0.3$ . This corresponds to  $\langle \eta \rangle = 10^{0.21z - 0.65}$ . These results are also supported by other indirect determinations of  $\eta$ . By requiring the mass function of relic black holes (as

<sup>9</sup> The bolometric corrections by Marconi et al. (2004) are roughly 2/3 of those by Elvis et al. (1994) and correspond to  $\log_{10} \left( \frac{L_{\text{bol}}}{10^{46} \text{ erg s}^{-1}} \right) = 0.37 - 0.40 (M_{b_J} + 25)$  with a scatter at fixed  $M_{b_J}$  of 0.3.

inferred from the X-ray background) to match its local counterpart, Marconi et al. (2004) found that  $0.1 \lesssim \eta \lesssim 1.7$  (with a preferred value of  $\eta \sim 0.5$ ). Once accounted for the different bolometric corrections, these values are in extremely good agreement with the results from McLure & Dunlop (2004). Similarly, Yu & Tremaine (2002) showed that the local mass density in black holes is consistent with the integrated luminosity density of quasars if they accreted mass nearly at the Eddington rate at redshifts  $z \gtrsim 2$ .

#### 4.1.4 The distribution of black-hole masses

The probability distribution of  $\log_{10} M_{\text{bh}}/M_{\odot}$  for a given  $L_{\text{bol}}$  is thus obtained by combining equation (22) with the observationally determined distribution of  $\eta$ :

$$P(\log_{10} \frac{M_{\text{bh}}}{M_{\odot}} | L_{\text{bol}}) = 0.73 \exp \left[ -\frac{(\log_{10} \frac{M_{\text{bh}}}{M_{\odot}} - f)^2}{0.6} \right] \quad (25)$$

with  $f = 8.70 - 0.21z + \log_{10}(L_{\text{bol}}/10^{46} \text{ erg s}^{-1})$ . For consistency, in order to estimate the black-hole mass associated with a quasar of given absolute magnitude  $M_{\text{b},j}$ , we combine equations (24) (including its associated scatter) and (25) which have been derived from the same dataset. This implies that a quasar with  $M_{\text{b},j} = -25$  corresponds to a mean black-hole mass of  $5.13 \times 10^8 M_{\odot}$  at  $z = 1$  and of  $3.16 \times 10^8 M_{\odot}$  at  $z = 2$ . Note that for the typical redshift and magnitude ranges spun by our sample,  $6 \times 10^7 M_{\odot} \lesssim \langle M_{\text{bh}} | M_{\text{b},j} \rangle \lesssim 3 \times 10^9 M_{\odot}$ . This interval is consistent with the masses inferred from dynamical measures in the local Universe (e.g. Tremaine et al. 2002 and references therein) and from the analysis of emission linewidths in the 2QZ (Corbett et al. 2003).

## 4.2 The mass of host haloes

Taking a step further, we can estimate the probability distribution that a quasar of a given luminosity is hosted by a dark-matter halo of mass  $M$ . Following Ferrarese (2002; see also Baes et al. 2003), this is obtained by assuming that a statistically significant correlation links  $M_{\text{bh}}$  and  $M$ .

Black-hole masses are found to be tightly correlated with the velocity dispersion of their host spheroid,  $\sigma_{\text{sph}}$  (Ferrarese & Merritt 2000; Gebhardt et al. 2000). The most recent determination considers  $\sim 30$  galaxies with secure detections of supermassive black holes (Tremaine et al. 2002). Observations also provide evidence for a correlation between  $\sigma_{\text{sph}}$  and the circular velocity in the flat part of the rotation curve of the host galaxy (Ferrarese 2002; Baes et al. 2003). By combining the  $M_{\text{bh}} - \sigma_{\text{sph}}$  and the  $\sigma_{\text{sph}} - v_c$  relations, Baes et al. (2003) find

$$\frac{M_{\text{bh}}}{M_{\odot}} = 10^{7.24 \pm 0.17} \left( \frac{v_c}{200 \text{ km s}^{-1}} \right)^{4.21 \pm 0.60}. \quad (26)$$

This purely observational relation can be used to link  $M_{\text{bh}}$  with the mass of the host halo. In order to do this, however, one needs to express  $v_c$  in terms of  $M$  which is a formidable task. As a first order approximation one can assume an equilibrium configuration for the dark-matter density profile in haloes. Both the singular isothermal sphere and models derived from numerical simulations (e.g. Navarro et al. 1997) provide good starting points. However, detailed modelling

of the rotation curve requires accounting for the distribution and physics of baryons (e.g. Mo, Mao & White 1998). In fact, the gas contribution can be dominant in the innermost regions of galaxies. Moreover, the condensation towards the centre of the dissipative material redistributes, through gravity, the collisionless matter.

For simplicity, we consider equilibrium profiles which only contain dark matter and we account for the presence of baryons in an approximate way. The circular velocity at the virial radius of each halo is

$$\frac{v_{\text{vir}}}{159.4 \text{ km s}^{-1}} = \left( \frac{M}{10^{12} h^{-1} M_{\odot}} \right)^{1/3} \left( \frac{E_z^2 \Delta_z}{18 \pi^2} \right)^{1/6}, \quad (27)$$

where  $E_z^2 = \Omega_0 (1+z)^3 + \Omega_{\Lambda}$ ,  $\Delta_z$  is the ratio between the mean density of the halo and the critical density of the Universe (both evaluated at redshift  $z$ ). For a spherical collapse, this function can be approximated as  $\Delta \simeq 18\pi^2 + 82x - 39x^2$  with  $x = \Omega_{\text{m}}(z) - 1$  and  $\Omega_{\text{m}}(z) = \Omega_0 (1+z)^3 / E_z^2$  (Bryan & Norman 1998).

A truncated singular isothermal sphere has a constant circular velocity profile  $v_c = v_{\text{vir}}$ , while for an NFW density profile

$$\frac{v_c(\mathcal{R})}{v_{\text{vir}}} = \left[ \frac{1}{\mathcal{R}} \frac{F(\mathcal{C} \cdot \mathcal{R})}{F(\mathcal{C})} \right]^{1/2}, \quad (28)$$

where  $\mathcal{R} = r/r_{\text{vir}}$ ,  $F(x) = \ln(1+x) - x/(1+x)$  and  $\mathcal{C}$  is the concentration parameter of the halo. In this case, the circular velocity vanishes when  $\mathcal{R} \rightarrow 0$ , reaches a maximum at  $\mathcal{R} \simeq 2.16/\mathcal{C}$  and matches the virial velocity at  $\mathcal{R} = 1$ . Two questions naturally arise: *i*) What is the value of  $\mathcal{R}$  which corresponds to the observed circular velocities? *ii*) What is the contribution of the baryons at this radius? These are the main uncertainties of our analysis.

For galaxies with HI rotation curves,  $v_c$  is typically measured at a few tens of kpc from the centre, well beyond the optical radius (a few kpc). On the other hand, the present-day virial radius of a halo with  $M = 10^{13} M_{\odot}$  is  $r_{\text{vir}} = 0.56$  Mpc. In other words, the largest scales sampled by rotation-curve measurements are nearly a factor of 10 smaller than the virial radius. Using galaxy-galaxy lensing data from the SDSS, Seljak (2002) has shown that, for galaxies above  $L_*$ ,  $v_c$  decreases significantly from the optical radius of a galaxy to the virial radius of its host halo. This result is independent of the morphological type and is probably suggesting that baryons contribute significantly to the circular velocity at the optical radius and that density profiles for the dark matter are highly concentrated (as expected in CDM models at  $z = 0$ ). Seljak (2002) also found a clear trend for the ratio  $\psi = v_c/v_{\text{vir}}$  with halo mass. Typical values are:  $\psi \sim 1.8$  for  $M \sim 3 \times 10^{11} M_{\odot}$ ,  $\psi \simeq 1.4 \pm 0.2$  for  $M \sim 10^{13} M_{\odot}$  and  $\psi < 1$  for cluster masses. This is in good agreement with the predictions of CDM models, since the dark matter concentration is expected to decrease with the halo mass and the baryonic contribution is expected to become less and less important.

Assuming that the observed  $v_c$  corresponds to the maximum value of the rotational velocity profile in an NFW halo tends to underestimate Seljak's results. Using equations (9) and (13) in Bullock et al. (2001), we find that, at  $z = 0$ , this assumption corresponds to  $\psi = 1.3$  ( $\mathcal{C} \sim 14$ ) for  $M \sim 3 \times 10^{11} M_{\odot}$  and  $\psi = 1.2$  ( $\mathcal{C} \sim 9$ ) for  $M \sim 10^{13} M_{\odot}$ . Anyway, these results show the correct trend with the halo

mass: smaller, more concentrated haloes are associated with larger values for  $\psi$ . It is worth noticing, however, that the candidate hosts of our quasars (haloes with  $M \sim 10^{13} M_\odot$  at  $0.8 < z < 2.1$ ) are expected to be much less concentrated ( $C \sim 3-5$ ) than their present-day counterparts. In this case, the maximum value of the rotational velocity is only 2-15 per cent higher than  $v_{\text{vir}}$ . This motivates the choice  $\psi \simeq 1$  as a viable alternative to the low-redshift results by Seljak (2002).

We have now collected all the elements necessary to estimate the probability distribution of the host-halo mass,  $M$ , for a quasar with given absolute magnitude  $M_{b_j}$ :  $\mathcal{P}(M|M_{b_j})$ . In brief: *i*) We assume that equations (24), (25) and (26), which have been determined at lower redshifts, are still valid for the host galaxies of our 2QZ quasars at  $0.8 < z < 2.1$ ; Their combination (including the scatter in each of them) is used to determine the probability distribution of  $v_c$ ; *ii*) We then convert circular velocities into halo masses by selecting a value of  $\psi$  and using equation (27). In what follows, to match the results by Seljak (2002), we assume a Gaussian distribution for  $\psi$  with mean value of 1.4 and scatter of 0.2 (case A); alternatively, based on the estimated low concentration of high-redshift haloes, we assume that  $\psi = 1$  (case B). These different choices bracket the range of plausible values for  $\psi$ .

### 4.3 The halo occupation number

By integrating over the luminosity function, the probability distribution  $\mathcal{P}(M|M_{b_j})$  can be easily turned into the mass function of dark haloes which are quasar hosts,

$$n_q(M, z) = \int_{M_{b_j}^f(z)}^{M_{b_j}^b(z)} \Phi(M_{b_j}, z) \mathcal{P}(M|M_{b_j}) dM_{b_j}. \quad (29)$$

The corresponding multiplicity function,  $M n_q(M, z)$ , is shown in the left panel of Fig. 3 for different values of  $z$ . Independently of redshift, the halo mass distribution per unit logarithmic interval of  $M$  peaks around  $10^{12.5-13} M_\odot$ : this is the characteristic mass of quasar hosts, whose value is in good agreement with those found in Section 3.3.2 (cf. Table 3). By then dividing  $n_q(M, z)$  by the halo mass function, a new estimate for the halo occupation number is obtained

$$N(M, z) = \frac{n_q(M, z)}{n(M, z)}. \quad (30)$$

Note that this, in principle, could give rise to a biased estimate of  $N(M, z)$ . In fact, in a CDM cosmology, each virialized halo contains a number of sub-haloes within its  $r_{\text{vir}}$ , and at least some of these sub-haloes will be associated with galaxies which formed within their local overdensities and then fell into the larger halo. Since the rotational properties of galaxies are expected to be related to local dark-matter overdensities, the values we derived for  $M$  in Section 4.2 most likely refer to sub-haloes. On the other hand,  $n(M)$  describes the mass distribution of the parent haloes. We can account for this problem by introducing the conditional mass function of the sub-haloes of mass  $M_s$  which lie within a parent halo of mass  $M_p > M_s$ ,  $n(M_s|M_p)$ . The probability that an halo with mass  $M$  is a parent one is then given by

$$\mathcal{P}_p(M) = \frac{n(M)}{n(M) + \int_M^\infty n(M_p) n(M|M_p) dM_p}, \quad (31)$$

where the integral at the denominator gives the mass function for the sub-haloes. We use two different functional forms for  $n(M_s|M_p)$  which have been derived from high-resolution numerical simulations (Sheth & Jain 2003; Vale & Ostriker 2004 and references therein). In both cases, we find that the sub-halo correction is negligibly small. In fact, at the redshifts spun by our quasar sample, the haloes we are considering are rather massive and only a few per cent of them have been included into larger units.

Results for the halo occupation number are presented in Fig. 3. In all cases, for  $M < 10^{14} M_\odot$ ,  $N(M)$  is well approximated by a broken power law. The low-mass tail has a typical slope  $\sim -3.6$  for case A and  $\sim -4.2$  for case B, independently of redshift. On the other hand, the high-mass tail gets progressively steeper when moving from low to high redshifts. For case A, we get a flat  $N(M)$  for the low-redshift sample, to be compared with a slope of  $\sim 0.4$  for the dataset at intermediate redshifts and of  $\sim 0.7$  for the highest-redshift quasars. The corresponding numbers for case B are  $\sim 0.4$ ,  $\sim 0.9$ ,  $\sim 1.1$ . For  $M > 10^{14} M_\odot$ , in both cases the halo occupation number starts growing exponentially. This happens because, in the high-mass tail,  $n_q(M, z)$  does not drop as fast as the exponential cutoff of the halo mass function (see the left panel in Fig. 3 and the shaded region in the right panel). Most likely this is a spurious effect due to the simple assumptions we use to derive  $n_q(M, z)$ . This artifact, however, does not affect our conclusions since the fraction of quasars that are found to reside in such massive haloes is extremely small (at most, a few  $\times 10^{-5}$  for case A and less than 2 per cent for case B).

Note that estimates for  $N(M)$  based on equation (30) are obtained without any information on the clustering properties of quasars. It is therefore interesting to check whether they are in agreement with the determination of  $\Xi^{\text{obs}}(r_\perp)$  we presented in Section 2.5. For this reason, we compute the effective bias associated with the different halo occupation numbers represented in Fig. 3. For the lowest-redshift sample, we get  $b_{\text{eff}} = 1.63$  (2.02) for case A (B). At intermediate redshifts, we find  $b_{\text{eff}} = 2.14$  (2.73) for case A (B). While, for the highest-redshift interval, we derive  $b_{\text{eff}} = 2.58$  (3.36) for case A (B). These numbers have to be compared with the observational results presented in Table 2. For case A, we note that, even though the estimated bias parameter increases with redshift (as like as the data in Table 2), its value is in general too low to accurately describe the observed clustering. In other words, case A tends to underestimate the mean mass of quasar host haloes. Predictions for case B, instead, are of better quality. In this case, our results for the bias parameter are rather accurate for the intermediate redshift sample, while they tend to overestimate (underestimate) the observational results at low (high) redshifts. Anyway, the bias inferred from our models is always acceptable (with respect to the statistical errors associated with the determinations of the projected correlation function). The maximum discrepancy appears at  $z_{\text{eff}} = 1.89$  and corresponds to a statistical significance of  $1.4\sigma$ . These results are in agreement with the recent analysis by Wyithe & Loeb (2004) who showed that quasar models with  $M_{\text{bh}} \propto v_c^5$ ,  $\psi = 1$  and  $\eta \sim 0.1 - 1$  are able to reproduce the evolution of the correlation length measured in a preliminary data release of the 2QZ (Croom et al. 2001, 2002). More accurate clustering measurements are then required to detect possi-

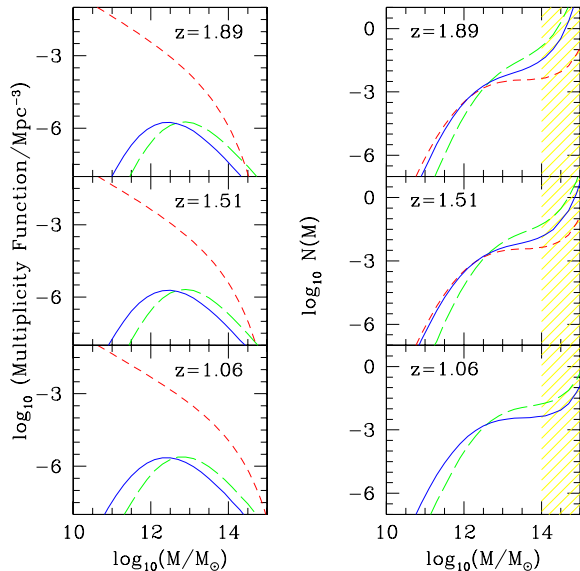


**Figure 3.** Left panel: the multiplicity function (differential number density per log-unit of mass and per unit volume) of haloes which are hosts of 2QZ quasars (continuous line for case A, long-dashed line for case B) is compared with the corresponding distribution for all the dark-matter haloes (short-dashed line) at different redshifts. Right panel: corresponding halo occupation numbers obtained by taking the ratio of the quasar-host mass function to the total halo mass function (continuous line for case A, long-dashed line for case B). For comparison, the case A solution at  $z = 1.06$  is reproduced with a short-dashed line in the two top panels.

ble changes in the  $M_{\text{bh}} - v_c$  correlation and to distinguish them from effects due to evolution of other parameters (for instance  $\eta$ ,  $\psi$  or the bolometric correction).

## 5 A PHENOMENOLOGICAL MODEL FOR QUASAR CLUSTERING

In Section 3.3.1 we presented a number of simple functional forms for the halo occupation number of quasars. In the absence of a physical model for quasar activity, there is no reason to prefer a given functional form for  $N(M)$  with respect to another if both can provide an acceptable description of the data. It is therefore interesting to consider a wider class of models which are theoretically sounded and that can be tested against observations. In this section, we discuss a new parameterization of the halo occupation number and we show how different observations constrain the parameters of the model. To find a non-degenerate solution we adopt an hybrid approach which combines the methods presented in Sections 3.3 and 4.2.

### 5.1 A more general halo occupation number

We consider here the “censored” power-law model,

$$N(M) = N_0 \left( \frac{M}{M_0} \right)^\alpha \Theta(M - M_0), \quad (32)$$

which has been widely used in the literature to describe galaxy clustering (e.g. Magliocchetti & Porciani 2003 and references therein). In this case, the halo occupation number vanishes for  $M < M_0$  and scales as a power law of the halo mass for  $M > M_0$ . The parameter  $N_0$  gives the mean number of objects contained in a halo of mass  $M_0$ .<sup>10</sup> Both hydrodynamical simulations and semianalytic models for galaxy formation are consistent with equation (32) (Sheth & Diaferio 2001; Berlind & Weinberg 2002; Berlind et al. 2003). We assume that the same parameterization is adequate for quasars. Given the correlation between black-hole and halo masses discussed in Section 4.2, for a quasar population with a given minimum luminosity, it is reasonable to expect the presence of a threshold mass for the host haloes. At the same time, a power-law scaling with an unspecified index  $\alpha$  for  $M > M_0$  is general enough to explore a wide range of possibilities. Note that models T and E presented in Section 3.3.1 are particular cases of equation (32). Moreover, the halo occupation number obtained in Section 4.3 by combining a set of empirical correlations is in qualitative agreement with equation (32):  $N(M)$  is well described by a power law with a low-mass cutoff.

As an additional test, in the Appendix, we use a publicly available semianalytic model for galaxy formation to show that equation (32) well approximates the halo occupation number of galaxies which, at  $z \sim 1$ , are actively forming stars in their bulges. Regrettably, since black-hole accretion is not accounted for in the semianalytic model, we have no way to tell whether these star-forming galaxies are also hosting active quasars. Even though imaged quasar hosts are consistent with being massive ellipticals (e.g. Dunlop et al. 2003), there is some observational evidence that, at high redshift, quasars might be associated with active star-formation (e.g. Omont et al. 2001; Hutchings et al. 2002). Moreover, in the local Universe, powerful Type 2 active galactic nuclei are found in bulges with either on-going star formation or young stellar populations (Kauffmann et al. 2003). Indeed, the observed correlation between black-hole mass and bulge velocity dispersion suggests that quasar activity and bulge formation probably are physically associated phenomena. For instance, galaxy interactions and bar-induced inflows might funnel some gas into the nuclear region of a galaxy thereby triggering simultaneous star formation and quasar activity. Even though such a reasoning is highly speculative, we find encouraging that equation (32) is in good agreement with the  $N(M)$  of synthetic galaxies which, at  $z \gtrsim 1$ , contain a substantial amount of cold gas in their nuclear region (and that, in principle, could be accreted onto supermassive black holes).

### 5.2 Constraints from large-scale clustering

Assuming equation (32), we apply the least-squares method introduced in Section 2.5 to determine the values of  $M_0$  and  $\alpha$  which best describe the clustering data presented in Fig. 1. Once again, we stress that the overall normalisation of

<sup>10</sup> Note that equation (32) is more general than the commonly used  $N(M) = (M/M_1)^\alpha \Theta(M - M_0)$  which, for  $\alpha = 0$ , automatically implies  $N(M) = 1$  at any  $M > M_0$ .

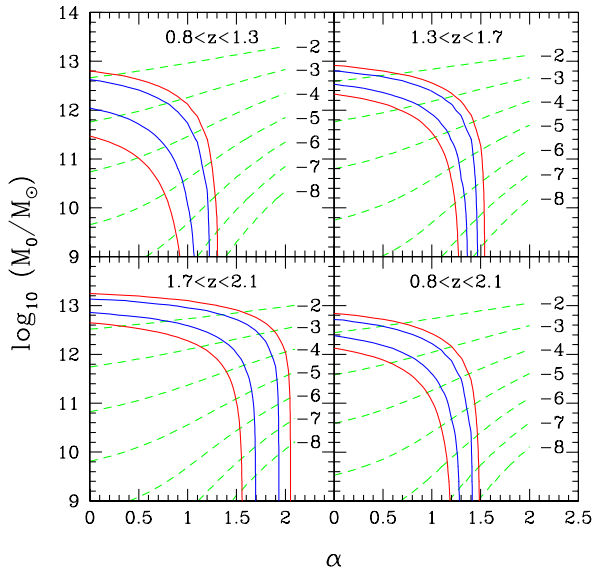


**Figure 4.** Contour levels of the  $\chi^2$  function for the parameters  $\alpha$  and  $M_0$  obtained by fitting the large-scale clustering of quasars in different redshift intervals with the predictions of the halo model given in equation (32). The various panels contain contour plots for the  $\chi^2$  surface in the  $\alpha - M_0$  plane. The contours correspond to  $\Delta\chi^2 = \chi^2 - \chi_{\min}^2 = 1$  and 4 (respectively marking the 68.3 and 95.4 per cent confidence levels for two fully degenerate Gaussian variables). Contours of the value of  $\log_{10} N_0$  which matches the observed number density are plotted as a function of  $\alpha$  and  $M_0$  (dashed lines with labels) for the different redshift bins considered.

$N(M)$  (e.g. the parameter  $N_0$ ) does not affect the shape and amplitude of  $\Xi(r_{\perp})$ .

We only consider the region of parameter space where  $\alpha \geq 0$  and  $M_0 \geq 10^9 M_{\odot}$ . We impose this lower limit to  $\alpha$  since we expect the halo occupation number to be a non-decreasing function of the halo mass.<sup>11</sup> On the other hand, we assume a lower limit for  $M_0$  because it is unreasonable to consider halo masses which are smaller than the minimum inferred mass of the black holes powering our quasars (cf. Section 4.1).

Contour plots of the  $\chi^2$  function are shown in Fig. 4. Note that, independently of the redshift interval, the region of parameter space allowed by the data is rather large and does not provide tight constraints on the values of  $M_0$  and  $\alpha$ . This is because our data only fix the normalisation of the correlation function (e.g. the bias parameter shown in Fig. 2) and there is a whole one-dimensional family of  $(\alpha, M_0)$  pairs which correspond to the same clustering amplitude.

<sup>11</sup> Note that solutions with  $\alpha < 0$  are allowed by the data if  $M_0 \sim 10^{12.5-13} M_{\odot}$  (the precise value slightly depending on the assumed redshift range). This solution for the halo occupation number implies quasars to be hosted by haloes lying in a narrow mass range. Since this is very similar to the model L we presented in Section 3.3.1, there is no need to rediscuss these solutions here.

### 5.3 Constraints from the number density

In the halo-model described by equation (32), the number density of quasars depends on all the free parameters  $\alpha$ ,  $M_0$  and  $N_0$ . In particular,  $N_0$  acts as an overall normalising factor so that, for given values of  $\alpha$  and  $M_0$ , it can be expressed in terms of the mean number density of quasars by combining equations (11) and (32). This gives an additional relationship among the parameters of the model as, for every  $(\alpha, M_0)$  pair, there is always a value of  $N_0$  which exactly matches  $n_{\text{QSO}}$ . The dashed lines in Fig. 4 show the regions in the  $(\alpha, M_0)$  plane where the observed density corresponds to a given value of  $\log_{10} N_0$  (indicated by the labels in the plot). The parameters  $N_0$  and  $M_0$  are strongly covariant: in order to get the right quasar abundance, one needs to lower the normalisation of the halo occupation number when  $M_0$  is reduced. The allowed range for  $N_0$  spans many orders of magnitude, reflecting the steep slope of the halo mass function at the low-mass end. It is worth noticing here that a low  $N_0$  corresponds to an extremely short quasar lifetime. Observations, however, set a lower limit for  $t_{\text{Q}}$ . In order to explain the proximity effect in the Ly- $\alpha$  forest, quasars have to maintain their ionizing luminosity for at least  $10^5$  yr (e.g. Bajtlik, Duncan & Ostriker 1988). This basically rules out all the models with  $M_0 \lesssim 10^{11} M_{\odot}$ . Future determinations of quasar radiative histories based on the transverse proximity effect (e.g. Adelberger 2004 and references therein) might give even more stringent limits.

As we already did in Section 3.3.2, we translate the assumed probability density function for the errors of the observed quasar number density into a likelihood function for the model parameters and we write

$$\mathcal{L}_{\text{tot}}(\alpha, M_0, N_0) = \mathcal{L}_{\text{clust}}(\alpha, M_0) \cdot \mathcal{L}_{\text{dens}}(\alpha, M_0, N_0). \quad (33)$$

This function will be extensively used in Section 5.5 to determine a non-degenerate solution for the quasar halo occupation number.

### 5.4 Constraints from small-scale clustering

For separations smaller than the typical size of the host haloes, the galaxy 2-point correlation function is dominated by the contribution of pairs lying within a single halo. In this regime,  $\xi(r)$  is fully described by equation (13) which encodes information on the halo occupation distribution through its second factorial moment,  $\Sigma^2(M)$ . This function can be conveniently expressed in terms of the halo occupation number as follows:

$$\Sigma^2(M) = \Gamma(M) N(M)^2. \quad (34)$$

For a Poisson distribution,  $\Gamma(M) = 1$  independently of  $M$ . In this case, measuring the 2-point correlation function on small scales provides additional constraints on the halo occupation number.

However, in general, the halo occupation distribution function is not Poissonian and  $\Gamma(M)$  depends on the halo mass. In principle, this complicates the estimate of  $N(M)$  from analyses of small-scale clustering. In fact, a number of additional free-parameters might be required to describe the behaviour of  $\Gamma(M)$ . On the other hand though, models of galaxy formation suggest that, independently of the galaxy sample considered,  $\Gamma(M)$  is a very simple function which

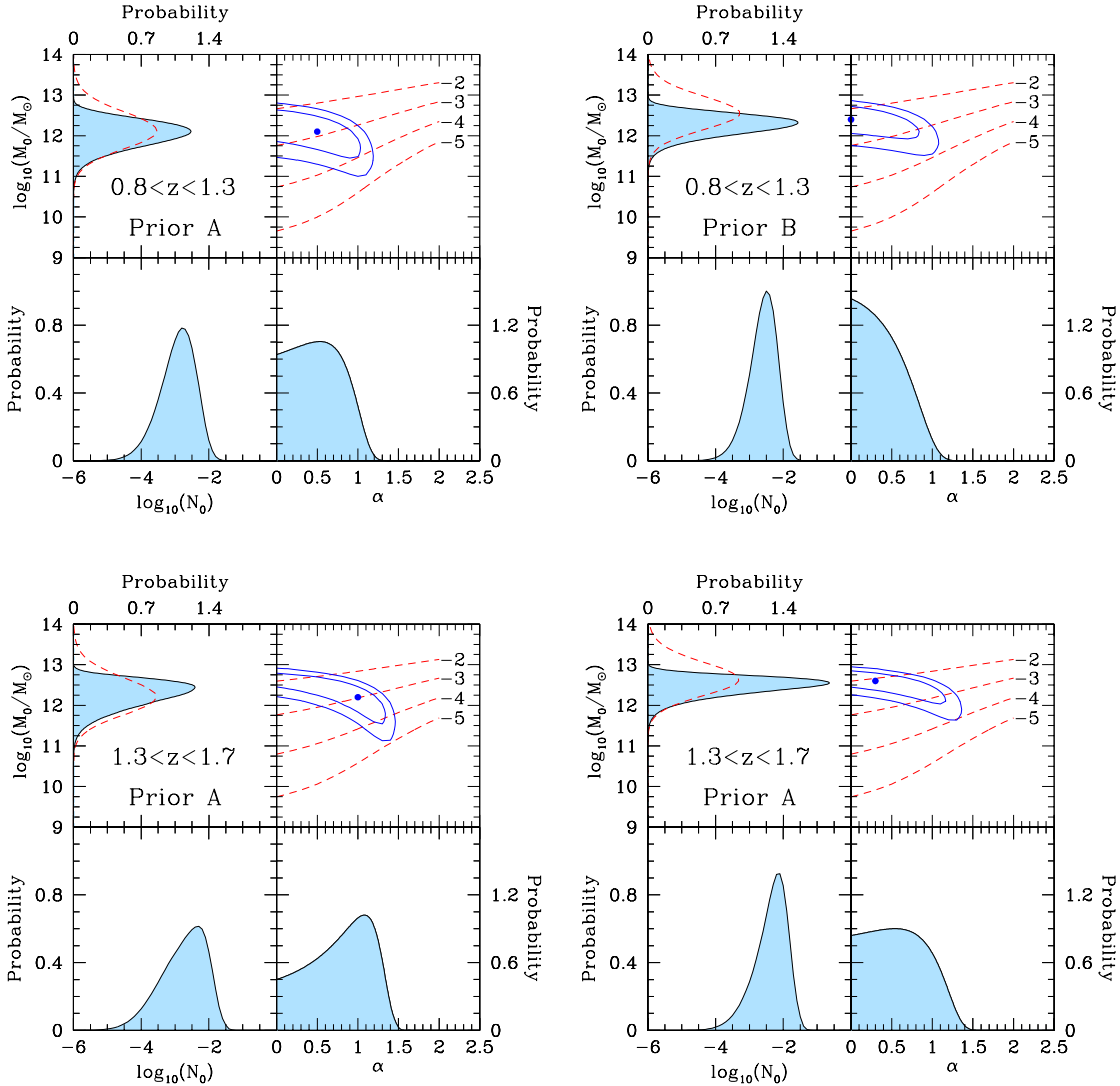


**Figure 5.** Posterior probability distribution for the parameters of the halo model. *Top-right:* Contours of the joint distribution of  $\alpha$  and  $M_0$  (obtained by marginalizing the three-dimensional posterior probability over  $N_0$ ). The most-probable point is marked with a small circle. To facilitate the comparison with Fig. 4, the continuous lines show the points where  $-0.5 \ln P_{\max}/P = 2.3$  and  $6.17$  (which, in this case, do not have any special meaning). As in Fig. 4, in order to represent the covariance of the different parameters, the dashed lines show the loci in the  $(\alpha, M_0)$  plane where a given value of  $\log_{10} N_0$  (indicated by the labels) perfectly matches the observed number density of quasars. *Other panels:* The probability densities for each single parameter (obtained by marginalizing the posterior distribution over the remaining two variables) are shown in the top-left (for  $\log_{10} M_0/M_\odot$ ), bottom-left (for  $\log_{10} N_0$ ) and bottom-right (for  $\alpha$ ) panels. In the top-left panels, the dashed lines show the assumed prior distribution for  $M_0$ .

can be parameterized in terms of the same variables that are used to describe  $N(M)$ . Consistent results have been obtained for local galaxies by using different semi-analytical models (e.g. Sheth & Diaferio 2001; Berlind & Weinberg 2002) and hydrodynamical simulations (Berlind et al. 2003). In all cases, the scatter of  $P_N(M)$  is strongly sub-Poissonian for haloes which, on average, contain less than 1 object, and nearly Poissonian for larger haloes. This property plays a fundamental role in breaking the degeneracy among all the models for the halo occupation number which can otherwise accurately describe galaxy clustering on large scales (Magliocchetti & Porciani 2003).

We do not know whether the same conclusions apply

to quasars. It is anyway interesting to understand what this would imply. Let us assume that, also for quasars,  $\Gamma \ll 1$  when  $N \ll 1$  while  $\Gamma \simeq 1$  when  $N \gtrsim 1$ . Within the allowed parameter range in Fig. 4, this implies that, at variance with galaxies, the 1-halo term never dominates the quasar correlation function even on scales which are much smaller than the typical halo size. This happens because the quasar  $N(M)$  is always much smaller than unity and its associated scatter is strongly sub-Poissonian. In other words, the distribution of (optically bright) quasars in a halo is binary (either there is one or there is none) and it is basically impossible to find 2 quasars being hosted by the same halo.

From the absence of quasar multiplets in a single halo



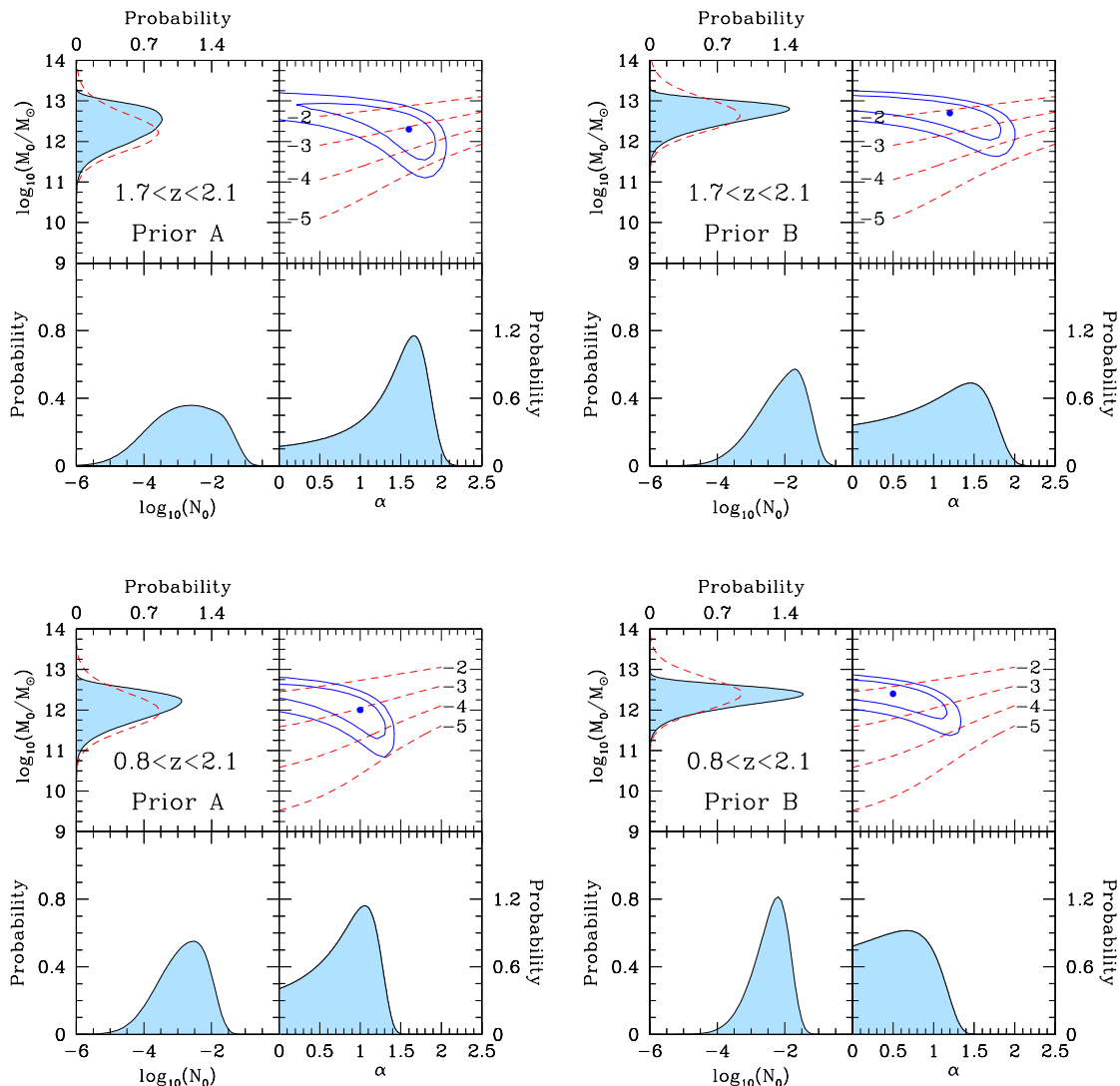


**Figure 6.** As in Fig. 5 but for different redshift ranges.

it follows that, in order to use observational determinations of quasar clustering on small scales to break the degeneracy among models which predict the same clustering amplitude on large scales, one has to rely on the detection of halo exclusion effects (different haloes cannot overlap). Note that this would be a direct “measure” of the spatial dimension of dark-matter haloes and therefore of their mass.

The exact signature induced by spatial exclusion is hard to predict since dark matter haloes are expected to be triaxial objects and the precise form of the quasar correlation function on small scales is also expected to depend on the position of each quasar within its host halo (see equation 13). However, it is clear that the configuration which maximizes this effect is obtained when quasars sit at the centre of the haloes. In this case, the distribution of quasars is a perfect (sparse sampled) tracer of the underlying halo distribution and the 2-point correlation function,  $\xi(r)$ , is expected to reach the value -1 on scales smaller than the typical size of the host halo. Such exclusion effects will then correspond to

a flattening of the projected function  $\Xi$  on the same scales. We note however that these effects might be hard to detect due to the small number statistics of close quasar pairs (cf. Fig. 1).

Similar arguments apply to any population of rare objects. A possible detection (with relatively low statistical significance) of exclusion effects has been reported from the analysis of the clustering properties of Lyman-break galaxies at redshift  $\sim 3$  (Porciani & Giavalisco 2002).

Note, however, that the scatter of the halo occupation distribution might depend on the detailed physical processes which give rise to the quasar phenomenon and thus be very different from the  $\Gamma$  function which describes the galaxy distribution. Therefore, the presence of quasar multiplets inside single haloes is not ruled out by the data. Measuring the quasar 2-point correlation function on separations smaller than  $1 h^{-1}$  Mpc would give a definitive answer to this question.

**Table 4.** Best-fitting values for the parameters of the halo model for different redshift ranges (superscript bf). The last three columns list the central 68.3 per cent credibility intervals for each single parameter. These have been obtained by marginalizing the posterior probability distribution function over the remaining parameters. The quoted values correspond to the 15.85, 50 and 84.15 percentiles. In the last column, we list the central 90 per cent credibility intervals for the quasar lifetime. We assume that a halo of  $2 \times 10^{13} M_{\odot}$  harbours, on average, a single super-massive black hole so that the halo occupation number of bright quasars coincides with their duty cycle.

$z_{\min}$	$z_{\max}$	Prior	$\log_{10}(M_0^{\text{bf}}/M_{\odot})$	$\alpha^{\text{bf}}$	$\log_{10} N_0^{\text{bf}}$	$\log_{10}(M_0/M_{\odot})$	$\alpha$	$\log_{10} N_0$	$t_{\text{Q}}/10^7 \text{ yr}$
0.8	1.3	A	12.1	0.5	-2.9	$12.1^{+0.3}_{-0.4}$	$0.5^{+0.3}_{-0.3}$	$-2.9^{+0.4}_{-0.6}$	$1.9^{+1.8}_{-1.3}$
0.8	1.3	B	12.4	0.0	-2.3	$12.2^{+0.2}_{-0.3}$	$0.4^{+0.3}_{-0.3}$	$-2.6^{+0.3}_{-0.5}$	$2.3^{+1.9}_{-1.4}$
1.3	1.7	A	12.2	1.0	-3.0	$12.3^{+0.3}_{-0.4}$	$0.8^{+0.4}_{-0.5}$	$-2.7^{+0.6}_{-0.8}$	$3.2^{+1.7}_{-1.6}$
1.3	1.7	B	12.6	0.3	-2.1	$12.5^{+0.2}_{-0.3}$	$0.6^{+0.4}_{-0.4}$	$-2.3^{+0.3}_{-0.6}$	$3.2^{+2.3}_{-1.5}$
1.7	2.1	A	12.3	1.6	-3.1	$12.4^{+0.4}_{-0.5}$	$1.4^{+0.4}_{-0.7}$	$-2.8^{+1.0}_{-1.1}$	$5.9^{+5.3}_{-2.4}$
1.7	2.1	B	12.7	1.2	-2.1	$12.7^{+0.3}_{-0.4}$	$1.1^{+0.5}_{-0.7}$	$-2.1^{+0.7}_{-0.8}$	$6.8^{+7.3}_{-2.9}$
0.8	2.1	A	12.0	1.0	-3.1	$12.1^{+0.3}_{-0.4}$	$0.8^{+0.3}_{-0.5}$	$-2.8^{+0.6}_{-0.8}$	$3.0^{+2.2}_{-1.8}$
0.8	2.1	B	12.4	0.5	-2.2	$12.3^{+0.2}_{-0.3}$	$0.6^{+0.4}_{-0.4}$	$-2.4^{+0.4}_{-0.6}$	$3.2^{+2.6}_{-1.9}$

### 5.5 Constraints from quasar luminosities

We have shown that, at variance with galaxy clustering, lack of information on the 2-point correlation function of quasars on small scales does not allow us to break the degeneracy among the best-fitting models presented in Fig. 4. We then use here information on quasar luminosities to further constrain the halo occupation model presented in equation (32).

In the Bayesian approach to statistics, the notion of probability of an hypothesis is admitted. Probabilities are then assigned to variables which are not intrinsically random but whose values are unknown. This is a way to quantify the degree of confidence dictated by the experimental evidence. It can be shown that probabilistic inference is adequate to deal with these quantities. Suppose that we want to use some experimental data  $\mathbf{D}$  to estimate the parameter vector  $\theta$  of an assumed model  $H$ . According to Bayes' theorem, the posterior (i.e. which accounts for the information contained in the experimental results) probability distribution for  $\theta$  is given by

$$P(\theta|\mathbf{D}, H) = \frac{\mathcal{L}(\mathbf{D}|\theta, H) P(\theta|H)}{P(\mathbf{D}|H)}, \quad (35)$$

where the likelihood function  $\mathcal{L}(\mathbf{D}|\theta, H)$  expresses our knowledge of the experimental errors while the probability density function  $P(\theta|H)$  encodes any prior knowledge we have on the parameters in the considered model (i.e. what we knew before acquiring the new experimental results). The normalisation factor  $P(\mathbf{D}|H)$  gives the probability of getting the data within the model (when all the distributions are properly normalised to unity this parameter is called evidence and can be used to discriminate among different models).

We apply equation (35) to our dataset with the halo occupation number given in equation (32). For each redshift interval, the likelihood function of our model parameters coincides with  $\mathcal{L}_{\text{tot}}$  in equation (33). For simplicity, to express our lack of prior knowledge, we adopt constant (non-informative) prior distributions for  $\log_{10} N_0$  and  $\alpha$ . On the other hand, as a prior distribution for  $\log_{10}(M_0/M_{\odot})$ , we use

the probability distribution  $\mathcal{P}(M|M_{b_j}^{\text{max}})$  that we derived at the end of Section 4.2. This is the probability distribution of the halo masses which harbour the faintest quasars that can be detected in each 2QZ sample considered. This prior knowledge is based on the empirically determined correlation between black-hole masses and the velocity dispersion of the host bulges. As in Section 4.2, to test the robustness of our method with respect to underlying systematic uncertainties, we consider two different prior distributions corresponding to  $\psi = 1.4 \pm 0.2$  (Prior A) and  $\psi = 1$  (Prior B).

Contours of the posterior probability in the  $\alpha - M_0$  plane and the probability distribution of the single parameters (marginalized over the remaining ones) are shown in Figs 5 and 6. The corresponding best-fitting values and credibility intervals for the different parameters are listed in Table 4.

Note that adopting our informative prior on  $M_0$  is enough to break the degeneracy among the parameters of the best-fitting models. In practice, both priors exclude the region  $M_0 < 10^{11} M_{\odot}$  where haloes are too small to harbour bright quasars. This is sufficient to determine a non-degenerate solution for each redshift range. In general, the cutoff mass,  $M_0$ , has a very mild evolution with redshift. Using prior A, we get  $M_0 \sim (1 - 3) \times 10^{12} M_{\odot}$ , while, with prior B, we obtain  $M_0 \sim (2 - 5) \times 10^{12} M_{\odot}$ .<sup>12</sup> On the other hand, in order to match the rapidly evolving bias parameter of the three quasar samples with a nearly invariant  $M_0$ , the high-mass slope,  $\alpha$ , tend to become steeper and steeper with increasing  $z$ . This is in qualitative agreement with the results presented in Section 4.3. At  $z_{\text{eff}} = 1.06, 1.51$  and  $1.89$ , we respectively find  $\alpha \sim 0.5, 0.8$  and  $1.4$  for prior A, and  $\alpha \sim 0.4, 0.6$  and  $1.1$  for prior B. It is important to stress, however, that the parameter  $\alpha$  is typically poorly de-

<sup>12</sup> Note that  $M_0$  is only mildly covariant with the high-mass slope,  $\alpha$ , in the sense that slightly lower values for  $M_0$  are generally associated with larger values of  $\alpha$ .

terminated. Strictly speaking, the data just set an upper limit for it. The allowed range for the normalisation parameter  $N_0$  varies systematically with the assumed prior. In brief,  $N_0$  spans a broader range (approximately from  $3 \times 10^{-5}$  to  $2 \times 10^{-2}$ ) when prior A is used. On the other hand, with prior B, the probability distribution for  $N_0$  is more peaked and ranges from  $3 \times 10^{-4}$  to  $3 \times 10^{-2}$ . We note that, for both priors,  $N_0$  is less tightly determined for our high-redshift sub-sample.

### 5.6 Results for the quasar lifetime

In this section, we use the posterior probability distribution presented in Figs. 5 and 6 to determine the characteristic quasar lifetime. For each halo mass, we first compute the probability density function of the halo occupation number:

$$\mathcal{P}(N) = \int \delta[N - N(M; \theta)] P(\theta | \mathbf{D}, H) d^3\theta \quad (36)$$

where  $\delta(x)$  denotes the Dirac-delta distribution,  $\theta \equiv (\alpha, M_0, N_0)$  and  $N(M; \theta)$  is given in equation (32). The 5, 50 and 95 percentiles of this distribution are shown in Fig. 7 as a function of the halo mass. Note that results are nearly identical for the two considered priors. For haloes with  $M \simeq 10^{13} M_\odot$ , the occupation number is tightly constrained by the data. We thus estimate the characteristic quasar lifetime by assuming that, for these haloes,  $N = t_Q/t_H$ . Our results (see Table 4) are in good agreement with those presented in Section 3.3.3:  $t_Q$  increases with  $z$  (and/or with quasar luminosity) and typically lies between  $10^7$  and  $10^8$  yr.

Even though the determination of  $N(M)$  becomes more uncertain for  $M \gg 10^{13} M_\odot$ , our results suggest that the occupation number of quasars tends to increase with the halo mass. This, however, does not imply that  $t_Q$  augments as well. In fact, our estimates for the quasar lifetime are degenerate with the occupation number of supermassive black holes which, most likely, increases with the halo mass.

## 6 IS THE HALO OCCUPATION NUMBER EVOLVING?

The analysis presented in Section 5 is based on two basic assumptions: the halo model and an assumed functional form for  $N(M)$ , namely, equation (32). Within these working hypotheses, in the three-dimensional parameter space  $(\alpha, M_0, N_0)$  we identified a one-dimensional family of models which accurately fits the abundance and clustering properties of quasars in the 2QZ. Prior information on  $M_0$ , inferred from quasar luminosities, was used in Section 5.5 to remove the degeneracy between the model parameters.

In this section, we want to test whether quasar clustering (without any additional constraint from quasar luminosity) is consistent with a non-evolving model for  $N(M)$ . Indeed, the contours in Fig. 4 obtained for quasars at different redshifts tend to lie in the same region of the  $\alpha - M_0$  parameter space. This also applies to the halo occupation number of the entire quasar sample ( $0.8 < z < 2.1$ ). We then assume, as a working hypothesis, that the shape of the halo occupation number (parameterized by  $\alpha$  and  $M_0$ ) does not

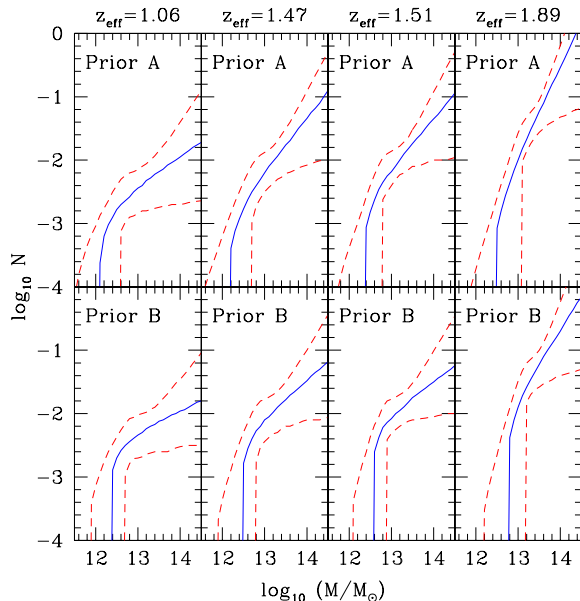


**Figure 7.** Halo occupation number obtained from the posterior probability distribution in Figs. 5 and 6. For each halo mass,  $M$ , we derive the probability density function of  $N$  using equation (36). Solid lines show the median occupation number as a function of  $M$  while dashed lines indicate the 5 and 95 percentiles of the distribution.

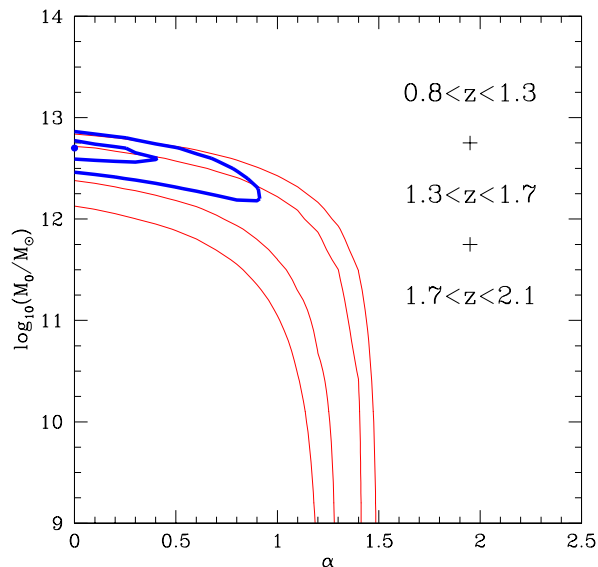


**Figure 8.** Contour levels for the  $\chi^2$  function obtained by combining the quasar sub-samples at different redshifts and assuming that the shape of the halo occupation number does not evolve with  $z$ . The  $\chi^2$  function is shown as a function of the halo model parameters  $\alpha$  and  $M_0$  and it has been minimized with respect to  $N_0^L$ ,  $N_0^M$  and  $N_0^H$ . A point indicates the best-fitting model while the heavy lines mark the 68.3 and 95.4 per cent confidence levels (respectively corresponding to  $\Delta\chi^2 = 2.3$  and 6.17). For ease of comparison, the contours presented in the bottom right panel of Fig. 4 are represented with light lines. These refer to the halo occupation number of our entire quasar sample in the redshift range  $0.8 < z < 2.1$ .

**Table 5.** Dependence of the best-fitting bias and halo-model parameters on  $\sigma_8$ . The entire quasar sample ( $0.8 < z < 2.1$ ) is considered here.

$\sigma_8$	$b$	model	$\log_{10} \frac{M_0}{M_\odot}$	$\log_{10} N_0$
0.7	$2.76 \pm 0.23$	T	$12.5^{+0.1}_{-0.2}$	$-1.8^{+0.2}_{-0.3}$
0.8	$2.42 \pm 0.20$	T	$12.6^{+0.1}_{-0.2}$	$-1.8^{+0.2}_{-0.3}$
0.9	$2.15 \pm 0.18$	T	$12.6^{+0.1}_{-0.2}$	$-1.9^{+0.2}_{-0.3}$
1.0	$1.91 \pm 0.16$	T	$12.7^{+0.1}_{-0.2}$	$-1.9^{+0.2}_{-0.3}$
0.7	$2.76 \pm 0.23$	E	$12.0^{+0.2}_{-0.4}$	$-2.9^{+0.3}_{-0.5}$
0.8	$2.42 \pm 0.20$	E	$12.0^{+0.2}_{-0.4}$	$-3.1^{+0.3}_{-0.5}$
0.9	$2.15 \pm 0.18$	E	$11.9^{+0.2}_{-0.4}$	$-3.3^{+0.3}_{-0.5}$
1.0	$1.91 \pm 0.16$	E	$11.7^{+0.2}_{-0.4}$	$-3.6^{+0.4}_{-0.6}$

evolve within the time-interval span by our quasar dataset. On the other hand, we let the overall normalisation  $N_0$  vary. In fact, because of selection effects, quasars lying at higher redshifts tend to be (on average) intrinsically brighter than their lower-redshift counterparts (cf. Table 1). Therefore, since we are considering objects within different luminosity ranges, it is reasonable to assume that they will correspond to different values of  $N_0$  and, thus, to different number densities. We denote these new parameters as  $N_0^L$ ,  $N_0^M$  and  $N_0^H$  respectively for the low, median and high redshift samples.

In Fig. 8, we show the confidence levels in the  $(\alpha, M_0)$  plane obtained by combining the three redshift subsamples. The objective function (total  $\chi^2$ ) has been computed by adding together the  $\chi^2$ s of each sample. The contours shown in the figure are obtained by minimizing the total  $\chi^2$  function over the different  $N_0^i$ s (we remind the reader that for each pair of values for  $(\alpha, M_0)$  it is always possible to choose the  $N_0^i$ s so that to perfectly match the observed densities).

The minimum value assumed by the total  $\chi^2$  function over the parameter space is 10.98 with 10 degrees of freedom. Therefore, assuming Gaussian errors, our working hypothesis that the halo occupation number of bright quasars does not evolve with redshift is not rejected by the data at any significant confidence level. The best fitting values for the parameters are:  $\alpha = 0.0^{+0.4}$ ,  $M_0 = 12.7 \pm 0.1$ ,  $\log_{10} N_0^L = -1.96^{+0.14}_{-0.26}$ ,  $\log_{10} N_0^M = -1.86^{+0.15}_{-0.24}$  and  $\log_{10} N_0^H = -1.73^{+0.17}_{-0.27}$ . All the quoted intervals correspond to  $\Delta\chi^2 = 1$ . This corresponds to  $b_{\text{eff}} = 2.08 \pm 0.10$ ,  $2.64 \pm 0.15$  and  $3.20 \pm 0.20$  respectively for the low, medium and high redshift samples. In this case then, changes in the bias parameter are merely driven by the joint time evolution of the halo population and of the mass autocorrelation function.

In summary, the combined dataset is consistent with a model for the halo occupation number which does not evolve with lookback time and exhibits a very shallow dependence on the halo mass ( $\alpha < 1$ , with values near zero which are favoured). One also finds  $M_0 \simeq 5 \times 10^{12} M_\odot$  and  $N_0^i \simeq 0.01 - 0.02$ . For all the quasar sub-samples, this corresponds to  $t_Q \simeq (3 - 4) \times 10^7$  yr.

## 7 DISCUSSION

### 7.1 Comparison of results

In Sections 3.3.2, 4.3, 5.5 and 6 we derived the quasar halo occupation number using a few different methods. The corresponding outcomes are fully consistent with each other. In all cases, we find that bright quasars are hosted by massive haloes with  $M \gtrsim 10^{12} M_\odot$ . For larger halo masses, the shape of the halo occupation number is not well constrained by the observational data and a wide range of possibilities is allowed. However, independently of the model details, we find that quasar hosts have characteristic masses of a few  $\times 10^{13} M_\odot$ . This is the key result of this analysis which strongly constrains quasar formation models. For instance, by coupling hydrodynamical simulations of galaxy formation with simple recipes for AGN activation, Di Matteo et al. (2003) recently concluded that quasar hosts at  $z \sim 2$  have typical masses of  $\sim 4 \times 10^{12} M_\odot$ . The corresponding clustering amplitude ( $b \sim 1.6$  at  $z = 1.89$ ) is too low to match our measures ( $b = 3.9 \pm 0.3$  at  $z_{\text{eff}} = 1.89$ ), thus suggesting that some revision of the model is probably required.

On the other hand, our findings are in good agreement with the typical mass of haloes hosting local radio galaxies (Magliocchetti et al. 2004). This further strengthens the connection between active galactic nuclei which exhibit different observational properties.

### 7.2 Control of systematics

A number of assumptions have been used in the present study. We discuss here how possible sources of systematic errors might affect our results.

All our analysis is developed within a specified cosmological framework based on the CDM paradigm. Modifying the cosmological parameters within the ranges allowed by recent CMB studies (e.g. Tegmark et al. 2004) induces minor changes in our conclusions. Results similar to those presented here are also obtained by slightly altering the power spectrum of density fluctuations. For instance, neglecting the presence of baryons (i.e. modifying the shape parameter of the linear power spectrum from 0.16 to 0.21) increases the bias parameters of our sub-samples by  $\sim 7$  per cent. In consequence, our best-fitting values for  $\alpha$  increase by 0.2-0.3. At the same time, for a given  $\alpha$ , the best-fitting values for  $\log_{10} M_0$  and  $\log_{10} N_0$  increase by 0.2-0.4.

The normalisation of the linear power spectrum of density fluctuations is still very controversial: estimates of  $\sigma_8$  from weak-lensing and cluster abundances range between 0.7 and 1 (see e.g. Table 4 in Tegmark et al. 2004 for a list of the most recent determinations). In Table 5, we use our entire sample of quasars to show how the best-fitting parameters for models T and E (cf. Section 3.3.1) change with  $\sigma_8$ . Note that, while the estimated bias parameter and  $\sigma_8$  are inversely proportional, the best-fitting parameters of the halo model depend only slightly on the assumed value for  $\sigma_8$  (compared with their statistical uncertainty).

Our analysis relies on a set of fitting functions calibrated on numerical simulations. These have been used to compute the mass function and bias parameter of dark matter haloes and the non-linear power spectrum of density fluctuations. Considering all the uncertainties, we estimate that,

on the scales considered here, the accuracy of the resulting correlation function is of the order of 10-20 per cent. This is still smaller than the statistical error associated with the observed correlation function. In consequence, we do not expect our results to be significantly affected by this source of systematic errors.

We used the most recent observational determinations of the Eddington ratio and of the correlation between  $M_{\text{bh}}$  and  $v_c$  to estimate the mass function of quasar host haloes. What is the sensitivity of our results on these assumptions? Assuming that all high-redshift quasars shine at the Eddington luminosity (which is a bit extreme but certainly plausible) would decrease our estimates for  $M_{\text{bh}}$  by a factor 2-3 and the mass of the host-haloes by a factor of 3-5. The best-fitting solutions for  $N(M)$  would then correspond to values for  $\alpha$  which are slightly larger than those presented in Section 5.5.

A large fraction of quasar-host galaxies are morphologically disturbed or interacting. This suggests that efficient black-hole fueling is triggered by galaxy encounters involving at least one gas rich object. Based on this, Kauffmann & Haehnelt (2000) developed a merger-based prescription of AGN activation. In our analysis, we never distinguish between merging and non-merging haloes. Can this bias our results? Previous studies have shown that, at  $z \sim 2$ , merging and randomly selected haloes of the same mass have the same clustering properties (Kauffmann & Haehnelt 2002; Percival et al. 2003). This implies that our results are valid also in the merger-driven scenario for AGNs. However, if quasars are indeed found only in merging haloes, our estimates for  $t_Q$  should be revised upwards by a factor of  $f_{\text{mer}}^{-1}$  with  $f_{\text{mer}}$  the fraction of merging haloes.

### 7.3 Number-density evolution: implications for high-redshift quasars

It is interesting to study how the number density of quasars with a given halo occupation number evolves. This is shown in Fig. 9 for different halo models. In all cases, the number density rapidly drops with redshift as a consequence of the hierarchical assembly of dark-matter haloes. On the other hand, by integrating the 2QZ luminosity function (Croom et al. 2004) above a given threshold value, one finds that, between  $0.4 < z < 2.1$ , the comoving number density of quasars increases with lookback time (see Fig. 9). This is clearly seen also in Table 1: both our low-redshift sub-sample and our full sample roughly correspond to  $M_{b_j} < -22.5$  but the quasar number density at  $z_{\text{eff}} = 1.47$  is a factor 1.3 higher than at  $z_{\text{eff}} = 1.06$ . We then conclude that, at  $z < 2$  and for a given luminosity threshold, the quasar halo occupation number cannot keep constant with time: at least its overall normalisation,  $N_0$ , (and the corresponding quasar lifetime) has to increase with  $z$ . This is probably due to the fast depletion of the gas available for accretion onto supermassive black holes during the late stages of galaxy and group formation (e.g. Cavaliere & Vittorini 2000). Once again it is important to stress the different nature of the halo-model parameters. Basically, while  $M_0$  determines which haloes are capable of hosting supermassive black holes,  $N_0$  and  $\alpha$  fix the overall normalisation and the scaling of the halo occupation number with the halo mass. These two parameters are probably more influenced (with

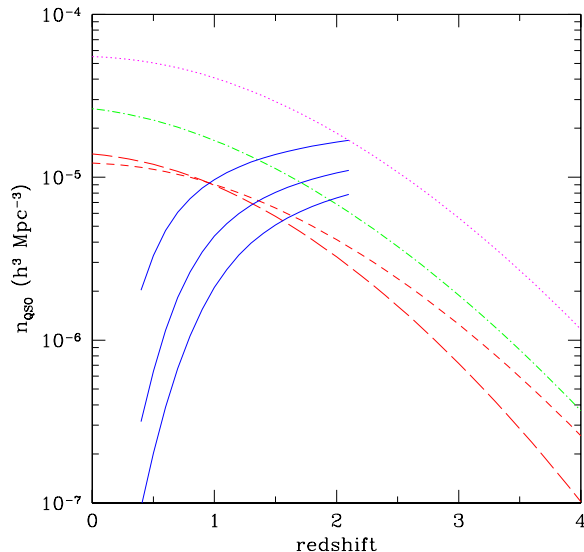


**Figure 9.** Number-density evolution of optically bright quasars. The solid lines are obtained using the best-fitting luminosity function from the 2QZ (Croom et al. 2004). From top to bottom they refer to  $M_{b_j} < -22.5, -23.6, -24.1$  (which correspond to the faintest objects in our sub-samples). The remaining lines show the evolution of  $n_{\text{QSO}}$  corresponding to a fixed halo occupation number. Two best-fitting models for  $N(M)$  at  $z_{\text{eff}} = 1.06$  are represented with dashed lines: namely, the Prior B solution discussed in Section 5.5 (short-dashed) and the non-evolving model presented in Section 6 (long-dashed). The dot-dashed line shows the best-fitting (Prior B) model for our full sample. The dotted line is obtained by renormalising the short-dashed line so to fit the 2QZ data at  $z = 2.1$  (which corresponds to  $\log_{10} N_0 = -1.65$ ).

respect to  $M_0$ ) by the local physics which determines the efficiency of gas accretion.

It is reasonable to expect that a fixed halo occupation number might accurately describe the quasar density evolution at higher redshifts when gas is ubiquitously available within massive dark matter haloes. Indeed, there is a consensus that the comoving number density of optically selected quasars peaks at  $z \sim 2 - 3$  and drops rapidly at higher redshifts. A number of factors (namely, observational incompleteness, uncertainties in the K-corrections and the possibility that a large fraction of quasars is not detectable in the optical band due to dust extinction) could generate a spurious drop but it is widely believed that at least part of the observed decrease is real (see e.g. the discussion in Fan et al. 2001). In Fig. 10, we compare the density evolution predicted by the halo model with observational data from the 2QZ and the SDSS Quasar Survey. For simplicity, we use the T model introduced in Section 3.3.1 and we assume that its parameters do not evolve with time. We find that the observed evolution of the quasar number density at  $z \sim 4$  (Fan et al. 2001) is consistent with a model where  $M_0 \gtrsim 10^{12} M_{\odot}$ . Similar values for  $M_0$  are also acceptable for a brighter sample of *i*-dropout objects detected at  $z \sim 6$  (Fan et al. 2004). Taking, for instance,  $M_0 = 10^{12} M_{\odot}$  requires  $N_0 = 3.8 \times 10^{-4}$  to fit the data at  $z = 4$ . This corresponds to  $b = 5.0$ ,  $r_0 = 6.7 h^{-1} \text{ Mpc}$ ,  $\langle M \rangle = 1.8 \times 10^{12} M_{\odot}$  and  $t_Q = 2.5 \times 10^5 \text{ yr}$ . Assuming

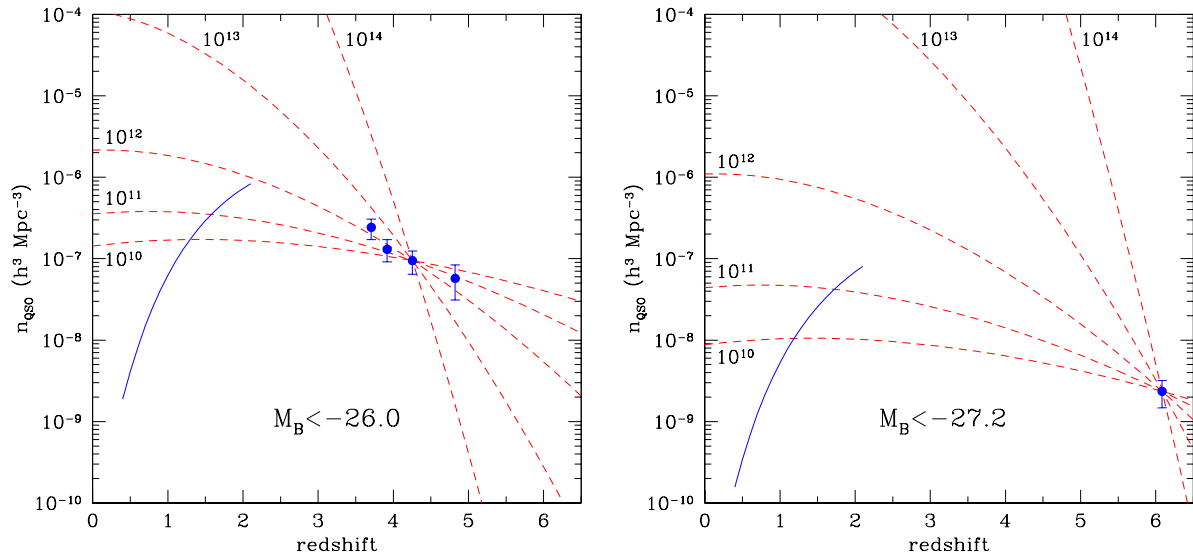


**Figure 10.** Number-density evolution of optically bright quasars. The left and right panels refer to different luminosity thresholds in the  $B$ -band as indicated in the figures. Datapoints with errorbars show the high-redshift results from the SDSS Quasar Survey (Fan et al. 2001; Fan et al. 2004). The solid lines are obtained using the best-fitting luminosity function from the 2QZ (Croom et al. 2004). The dashed lines refer to halo occupation models of the form  $N(M) = N_0 \cdot \Theta(M - M_0)$ . The adopted values for  $M_0$  are indicated in the figure and  $N_0$  is fixed so to match the observed quasar density at  $z \sim 4$  (left panel) and  $z \sim 6$  (right panel).

that equation (26) still holds at  $z = 4$ , from the estimated  $\langle M \rangle$ , we obtain  $M_{\text{bh}} = 1.2 \times 10^8 M_\odot$  which implies a super-Eddington accretion rate with  $\eta = 2.8$ . On the other hand, choosing  $M_0 = 10^{13} M_\odot$  gives  $N_0 = 0.18$ ,  $b = 9.2$ ,  $r_0 = 14 h^{-1} \text{Mpc}$ ,  $\langle M \rangle = 1.4 \times 10^{13} M_\odot$  and  $t_Q = 1.3 \times 10^8 \text{yr}$ . This corresponds to  $M_{\text{bh}} = 2.1 \times 10^9 M_\odot$  and  $\eta = 0.16$ . This clearly shows how future clustering measurements will be crucial to studying the physical properties of high-redshift quasars. The low abundance of optically bright objects, however, poses enormous difficulties for this kind of studies.

## 8 SUMMARY

We have used a flux limited sample of  $\sim 14,000$  2QZ quasars with  $M_{b_j} < -22.5$  to study the quasar clustering properties in the redshift range  $0.8 < z < 2.1$ . Our main results are summarized as follows.

(i) For spatial separations between 1 and  $20 h^{-1} \text{Mpc}$ , the correlation function for our whole quasar sample (corresponding to an effective redshift  $z_{\text{eff}} = 1.47$ ) is well approximated by a power law with slope  $\gamma = 1.53 \pm 0.20$  and comoving correlation length  $r_0 = 4.8^{+0.9}_{-1.5} h^{-1} \text{Mpc}$ .

(ii) Splitting the sample into three redshift ranges, we find evidence for an increase of the clustering amplitude with lookback time. The correlation function for quasars at  $1.7 < z < 2.1$  ( $z_{\text{eff}} = 1.89$ ) is nearly a factor of 2 higher with respect to the whole sample ( $z_{\text{eff}} = 1.47$ ). Since flux-limited surveys tend to select intrinsically brighter objects at higher-redshifts, it is not possible to tell, however, whether this effect is due to real evolution of the quasar population or to luminosity dependent clustering. We will further address this issue in a future paper.

(iii) For all the sub-samples, the correlation function

is well approximated by a power law. The best-fitting parameters, which are strongly covariant (see Fig. 1), range between  $-2.0 \lesssim \gamma \lesssim -1.5$  and  $4 \lesssim r_0/h^{-1} \text{Mpc} \lesssim 8$  (see Table 2). Within the statistical uncertainties, data in different redshift bins can be anyway described by the same value of  $\gamma$ . Assuming that the slope of the correlation function does not change with redshift, evolution of the correlation length is detected at the  $3.6\sigma$  confidence level.

(iv) Within the framework of concordance cosmology, high-redshift quasars are more biased tracers of the mass distribution than their low-redshift counterparts. The observed quasar-to-mass bias parameter is consistent with being scale-independent for the separations probed by our analysis. Assuming  $\sigma_8 = 0.8$ , we obtain  $b = 2.42^{+0.20}_{-0.21}$  for the whole quasar sample. On the other hand, we find  $b = 1.80^{+0.20}_{-0.24}$  for  $0.8 < z < 1.3$ ,  $b = 2.62^{+0.18}_{-0.19}$  for  $1.3 < z < 1.7$  and  $b = 3.86^{+0.32}_{-0.35}$  for  $1.7 < z < 2.1$ . In hierarchical models for structure formation, the bias parameter of a population of tracers can be readily linked to the mass of their host dark-matter haloes. At a given  $z$ , values of  $b$  which are significantly larger than unity correspond to haloes with  $M \gg M_*(z)$  where  $M_*(z)$  denotes the characteristic mass of haloes which are forming at that epoch out of  $1\sigma$  density fluctuations. The bias parameters of our sub-samples then suggests that quasars are hosted by rare, massive haloes.

(v) Considering three different versions of the halo model, we find that the observed quasar number density and clustering amplitude are consistent with a picture where: (a) quasars form in haloes with  $M > 10^{12} M_\odot$ ; (b) the mean mass of their host haloes is a few  $\times 10^{13} M_\odot$ . This result is independent of the detailed form of the halo occupation number and hence it can be used to constrain models of quasar formation.

(vi) Our best-fitting models at  $z_{\text{eff}} = 1.06$  suggest that

$N(M) \propto M^{0.4-0.5}$  for  $M > 10^{12} M_{\odot}$  and rapidly drops to zero for smaller values of  $M$ . For higher redshifts,  $N(M)$  tends to increase more rapidly with the halo mass. For instance, at  $z_{\text{eff}} = 1.89$ ,  $N(M) \propto M^{1-1.5}$  for  $M > 10^{13} M_{\odot}$ . It is worth stressing, however, that the data are also consistent with a non-evolving functional form for  $N(M)$  where quasars reside in haloes more massive than  $5 \times 10^{12} M_{\odot}$  and where the halo occupation number has a very weak dependence on the halo mass.

(vii) The mean number of quasars per halo is always smaller than one and typically lies between 0.01 and 0.1. Systematic searches for close pairs are needed to understand whether 2 active quasars can be hosted by a single halo.

(viii) The observed clustering evolution is consistent with assuming that the locally observed correlation between black-hole mass and host-galaxy circular velocity (Ferrarese 2002; Baes et al. 2003) is still valid at  $z > 1$ .

(ix) The fraction of potential host-haloes which indeed harbour a bright quasar increases from  $\lesssim 1$  per cent at  $z_{\text{eff}} = 1.06$  to 5–10 per cent at  $z_{\text{eff}} = 1.89$ . From this, we infer that the characteristic quasar lifetime  $t_Q$  increases with redshift (and/or with optical luminosity), ranging from a few  $\times 10^7$  yr at  $z \sim 1$  to  $\sim 10^8$  yr at  $z \sim 2$ . A number of assumptions (see Section 3.3.3) are used to derive this result which should therefore be regarded as an order of magnitude estimate.

In brief, this paper presents state-of-the-art measurements of quasar clustering and establishes an accurate benchmark for quasar-formation models. Future results from the SDSS quasar survey will provide an independent verification of our results and, thanks to the different quasar-selection criteria, will extend them to even higher redshifts.

## ACKNOWLEDGMENTS

CP and PN thank Simon Lilly for useful suggestions and comments. MM acknowledges Gianfranco De Zotti and Luigi Danese for many clarifying discussions. PN thanks Phil Outram and Tom Shanks for stimulating discussions about the 2QZ. CP and PN are supported by the Zwicky Prize fellowship program at ETH-Zürich. The 2dF QSO Redshift Survey (2QZ) was compiled by the 2QZ survey team from observations made with the 2-degree Field on the Anglo-Australian Telescope.

## REFERENCES

Adelberger K. L., 2000, in Mazure A., Le Fèvre O., Le Brun V., eds., ASP Conf. Ser. Vol. 200, Clustering at High Redshift, Astron. Soc. Pac., San Francisco, p. 13  
 Adelberger K. L., 2004, ApJ, in press, astro-ph/0405505  
 Adelberger K. L., Steidel C. C., Shapley A. E., Pettini M., 2003, ApJ, 584, 45  
 Andreani P., Cristiani S., 1992, ApJ, 398, L13  
 Andreani P., Cristiani S., Lucchin F., Matarrese S., Moscardini L., 1994, ApJ, 430, 458  
 Arnouts S., Cristiani S., Moscardini L., Matarrese S., Lucchin F., Fontana A., Giallongo E., 1999, MNRAS, 310, 54  
 Baes M., Buyle P., Hau G. K. T., Dejonghe H., 2003, MNRAS, 341, L44  
 Bahcall J. N., Kirhakos S., Saxe D. H., Schneider D. P., 1997, ApJ, 479, 642  
 Bajlik S., Duncan R. C., Ostriker J. P., 1988, ApJ, 327, 570

Bechtold J., Elvis M., Fiore F., Kuhn O., Cutri R. M., McDowell J. C., Rieke M., Siemiginowska A., Wilkes B. J., 1994, AJ, 108, 374  
 Berlind A. A., Weinberg D. H., 2002, ApJ, 575, 587  
 Berlind A. A. et al., 2003, ApJ, 593, 1  
 Blair M., Gilmore G., PASP, 94, 742  
 Brotherton M. S., Tran H. D., Becker R. H., Gregg M. D., Laurent-Muehleisen S. A., White R. L., 2001, ApJ, 546, 775  
 Bryan G. L., Norman M. L., 1998, ApJ, 495, 80  
 Bullock J. S., Wechsler R. H., Somerville R. S., 2002, MNRAS, 329, 246  
 Bullock J. S., Kolatt T. S., Sigad Y., Somerville R. S., Kravtsov A. V., Klypin A. A., Primack J. R., Dekel A., 2001, MNRAS, 321, 559  
 Carlberg R. G., Cowie L. L., Songaila A., Hu E. M., 1997, ApJ, 484, 538  
 Catelan P., Lucchin F., Matarrese S. & Porciani C., 1997, MNRAS, 297, 692  
 Cavaliere A., Vittorini V., 2000, ApJ, 543, 599  
 Coil A. L et al., 2004, ApJ, in press, astro-ph/0305586  
 Cole S., Kaiser N., 1989, MNRAS, 237, 1127  
 Colless M. et al., 2001, MNRAS 328, 1049  
 Corbett E. A., Croom S. M., Boyle B. J., Netzer H., Miller L., Outram P. J., Shanks T., Smith R. J., Rhook K., 2003, MNRAS, 343, 705  
 Cristiani S., Vio R., 1990, A&A, 227, 385  
 Croom S. M., Shanks T., 1996, MNRAS, 281, 893  
 Croom S. M., Shanks T., Boyle B. J., Smith R. J., Miller L., Loaring N. S., Hoyle F., 2001, MNRAS, 325, 483  
 Croom S. M., Boyle B. J., Loaring N. S., Miller L., Outram P. J., Shanks T., Smith R. J., 2002, MNRAS, 335, 459  
 Croom S. M., Smith R. J., Boyle B. J., Shanks T., Miller L., Outram P. J., Loaring N. S., 2004, MNRAS, 349, 1397  
 Daddi E., Broadhurst T., Zamorani G., Cimatti A., Röttgering H., Renzini, A., 2001, A&A, 376, 825  
 Di Matteo T., Croft R. A. C., Springel V., Hernquist L., 2003, ApJ, 593, 56  
 Dunlop J. S., McLure R. J., Kukula M. J., Baum S. A., O’Dea C. P., Hughes D. H., 2003, MNRAS, 340, 1095  
 Efstathiou G., 1998, in Lawrence A., eds., proc. 3rd IRAS conf., Comets to Cosmology, Springer, New York, p. 312  
 Elvis M., Risaliti G., Zamorani G., 2002, ApJ, 565, L75  
 Elvis M. W., Wilkes B. J., McDowell J. C., Green R. F., Bechtold J., Willner S. P., Oey M. S., Polomski E., Cutri R., 1994, ApJS, 95, 1  
 Enoki M., Nagashima M., Gouda N., 2003, PASJ, 55,133  
 Fabian A. C., Iwasawa K., 1999, MNRAS, 303, L34  
 Falomo R., Kotilainen J. K., Pagani C., Scarpa R., Treves A., 2004, ApJ, 604, 495  
 Fan X. et al. 2001, AJ, 121, 54  
 Fan X. et al. 2004, AJ, in press, astro-ph/0405138  
 Ferrarese L., 2002, ApJ, 578, 90  
 Ferrarese L., Merritt D., 2000, ApJ, 539, L9  
 Firth A. E et al., 2002, MNRAS, 332, 617  
 Gebhardt K. et al., 2000, ApJ, 539, L13  
 Granato G. L., De Zotti G., Silva L., Bressan A., Danese L., 2004, ApJ, 600, 580  
 Grazian A., Negrello M., Moscardini L., Cristiani S., Haehnelt M. G., Matarrese S., Omizzolo A., Vanzella E., 2004, AJ, 127, 592  
 Haehnelt M. G., Kauffmann G., 2000, MNRAS, 318, 35  
 Haehnelt M. G., Natarajan P., Rees M. J., 1998, MNRAS, 300, 817  
 Haiman Z., Hui L., 2001, ApJ, 547, 27  
 Hamilton A. J. S., 1993, ApJ, 417, 19  
 Hamilton T. S., Casertano S., Turnshek D. A., 2002, ApJ, 576, 61

- Hatton S., Devriendt J. E. G., Ninin S., Bouchet F. R., Guiderdoni B., Vibert D., 2003, *MNRAS*, 343, 75
- Hoyle F., Outram P. J., Shanks T., Croom S. M., Boyle B. J., Loaring N. S., Miller L., Smith R. J., 2002, *MNRAS*, 329, 336
- Hutchings J. B., Frenette D., Hanisch R., Mo J., Dumont P. J., Redding D. C., Neff S. G., 2002, *AJ*, 123, 2936
- Iovino A., Shaver P. A., 1988, *ApJ*, 330, L13
- Kaiser N., 1987, *MNRAS*, 227, 1
- Kauffmann G., Haehnelt M. G., 2000, *MNRAS*, 311, 576
- Kauffmann G., Haehnelt M. G., 2002, *MNRAS*, 332, 529
- Kauffmann G. et al., 2003, *MNRAS*, 346, 1055
- Kukula M. J., Dunlop J. S., McLure R. J., Miller L., Percival W. J., Baum S. A., O’Dea C. P., 2001, *MNRAS*, 326, 1533
- Lacey C., Cole S., 1993, *MNRAS*, 262, 627
- La Franca F., Andreani P., Cristiani S., 1998, *ApJ*, 497, 529
- Landy S. D., Szalay A. S., 1993, *ApJ*, 412, 64
- Le Fèvre O., Hudon D., Lilly S. J., Crampton D., Hammer F., Tresse L., 1996, *ApJ*, 461, 534
- Lynden-Bell D., 1969, *Nature*, 223, 690
- Madgwick D. S. et al., 2002, *MNRAS*, 333, 133
- Magliocchetti M., Maddox S., 1999, *MNRAS*, 306, 988
- Magliocchetti M., Porciani C., 2003, *MNRAS*, 346, 186
- Magliocchetti et al., 2004, *MNRAS*, in press, astro-ph/0312160
- Magorrian J. et al., 1998, *AJ*, 115, 2285
- Marconi A., Risaliti G., Gilli R., Hunt L. K., Maiolino R., Salvati M., 2004, *MNRAS*, in press, astro-ph/0311619
- Marinoni C., Hudson M. J., 2002, *ApJ*, 569, 101
- Martini P., Weinberg D. H., 2001, *ApJ*, 547, 12
- Matarrese S., Coles P., Lucchin F., Moscardini L., 1997, *MNRAS*, 286, 115
- McLure R. J., Dunlop J. S., 2004, *MNRAS*, submitted, astro-ph/0310880
- Menci N., Cavaliere A., Fontana A., Giallongo E., Poli F., Vitorini V., 2003, *ApJ*, 587, 63
- Mo H. J., Fang L. Z., 1993, *ApJ*, 410, 493
- Mo H. J., White S. D. M., 1996, *MNRAS*, 282, 347
- Mo H. J., Mao S., White S. D. M., 1998, *MNRAS*, 295, 319
- Monaco P., Salucci P., Danese L., 2000, *MNRAS*, 311, 279
- Moscardini L., Matarrese S., Lucchin F., Rosati P., 2000, *MNRAS*, 316, 283
- Moustakas L., Somerville R. S., 2002, *ApJ*, 577, 1
- Navarro J.F., Frenk C.S., White S.D.M., 1997, *ApJ*, 490, 493
- Norberg P. et al. 2002a, *MNRAS*, 332, 827
- Norberg P. et al. 2002b, *MNRAS*, 336, 907
- Omont A., Cox P., Bertoldi F., McMahon R. G., Carilli C., Isaak K. G., 2001, *A&A*, 374, 371
- Outram P. J., Hoyle F., Shanks T., Croom S. M., Boyle B. J., Miller L., Smith R. J., Myers A. D., 2003, *MNRAS*, 342, 483
- Outram P. J., Shanks T., Boyle B. J., Croom S. M., Hoyle F., Loaring N. S., Miller L., Smith R. J., 2004, *MNRAS*, 348, 745
- Peacock J. A., Dodds S. J., 1996, *MNRAS*, 267, 1020
- Peacock J. A., Smith R. E., 2000, *MNRAS*, 318, 1144
- Percival W. J., Miller L., McLure R. J., Dunlop J. S., 2001, *MNRAS*, 322, 843
- Percival W. J., Scott D., Peacock J. A., Dunlop J. S., 2003, *MNRAS*, 338, L31
- Porciani C., Giavalisco M., 2002, *ApJ*, 565, 24
- Porciani C., Matarrese S., Lucchin F., Catelan P., 1998, *MNRAS*, 298, 1097
- Richstone D. et al., 1998, *Nature*, 395, A14
- Roche N. D., Dunlop J., Almaini O., 2003, *MNRAS*, 346, 803
- Salpeter E. E., 1964, *ApJ*, 140, 796
- Salucci P., Szuszkiewicz E., Monaco P., Danese L., 1999, *MNRAS*, 307, 637
- Schneider D. P. et al. 2003, *AJ*, 126, 2579
- Scoccimarro R., Sheth R. K., Hui L., Jain B., 2001, *ApJ*, 546, 20
- Seljak U., 2000, *MNRAS*, 318, 203
- Seljak U., 2002, *MNRAS*, 334, 797
- Shanks T., Boyle B. J., 1994, *MNRAS*, 271, 753
- Shanks T., Fong R., Boyle B. J., Peterson B. A., 1987, *MNRAS*, 227, 739
- Shaver P. A., 1984, *A&A*, 136, L9
- Sheth R. K., Tormen G., 1999, *MNRAS*, 308, 119
- Sheth R. K., Diaferio A., 2001, *MNRAS*, 322, 901
- Sheth R. K., Jain B., 2003, *MNRAS*, 345, 529
- Silk J., Rees M. J., 1998, *A&A*, 331, L1
- Tegmark M. et al., 2004, PRD in press, astro-ph/0310723
- Tremaine S. et al., *ApJ*, 2002, 574, 740
- Vale A., Ostriker J. P., 2004, *MNRAS*, submitted, astro-ph/0402500
- van den Bosch F. C., Mo H. J., Yang X., 2003, *MNRAS*, 345, 923
- Yamamoto K., Suto Y., 1999, *ApJ*, 517, 1
- Yang X., Mo H. J., van den Bosch F. C., 2003, *MNRAS*, 339, 1057
- Yu Q., Tremaine S., 2002, *MNRAS*, 335, 965
- Wyithe J. S. B., Loeb A., 2003, *ApJ*, 595, 614
- Wyithe J. S. B., Loeb A., 2004, *ApJ*, submitted, astro-ph/0403714
- Zehavi I. et al., 2003, astro-ph/0301280
- Zel’dovich Ya. B., Novikov I. D., 1964, *Soviet Phys. Dokl.*, 158, 811
- Zheng Z., 2004, *ApJ*, in press, astro-ph/0307030

## APPENDIX A: THE HALO OCCUPATION DISTRIBUTION FROM SEMI-ANALYTIC MODELS OF GALAXY FORMATION

We use here semi-analytic models of galaxy formation to get an insight into the problem of choosing a functional form for the first two moments of the quasar halo occupation distribution. What we are after is a simple parameterization of the functional dependence of  $N(M)$  and  $\Sigma^2(M)$ . Note that we just want to determine the “shape” of these functions, and we have no interest in the values of the free parameters which best fit the semi-analytic data.

### A1 The halo occupation number

A number of authors introduced simplified schemes to include quasar activity in galaxy formation models (e.g. Kauffmann & Haehnelt 2002; Enoki, Nagashima & Gouda 2003; Menci et al. 2003; Di Matteo et al. 2003 and references therein). In most cases, the formation and fuelling of supermassive black holes is associated with galaxy interactions and merging. Regrettably, to the best of our knowledge, mock catalogues produced with these models are not publicly available.

There is evidence that, at high redshift, quasars are associated with star-forming galaxies (e.g. Omont et al. 2001; Hutchings et al. 2002). It is then plausible to expect that the halo-occupation properties of quasars might share some similarities with those of galaxies which show active star formation in their central regions. As an example, here we use the semi-analytic models of the GalICS I collaboration (Hatton et al. 2003) to study the halo occupation number of galaxies which at  $z = 1.08$  (roughly corresponding to the median value for our low-redshift sample) are actively forming stars in their bulges. Note that, because of numerical resolution effects, halo masses in these semianalytic models have to be larger than  $1.66 \times 10^{11} M_{\odot}$  (corresponding to 20 particles in the N-body simulation used to determine the halo merger trees). Results are shown in Fig. A1. The left panel



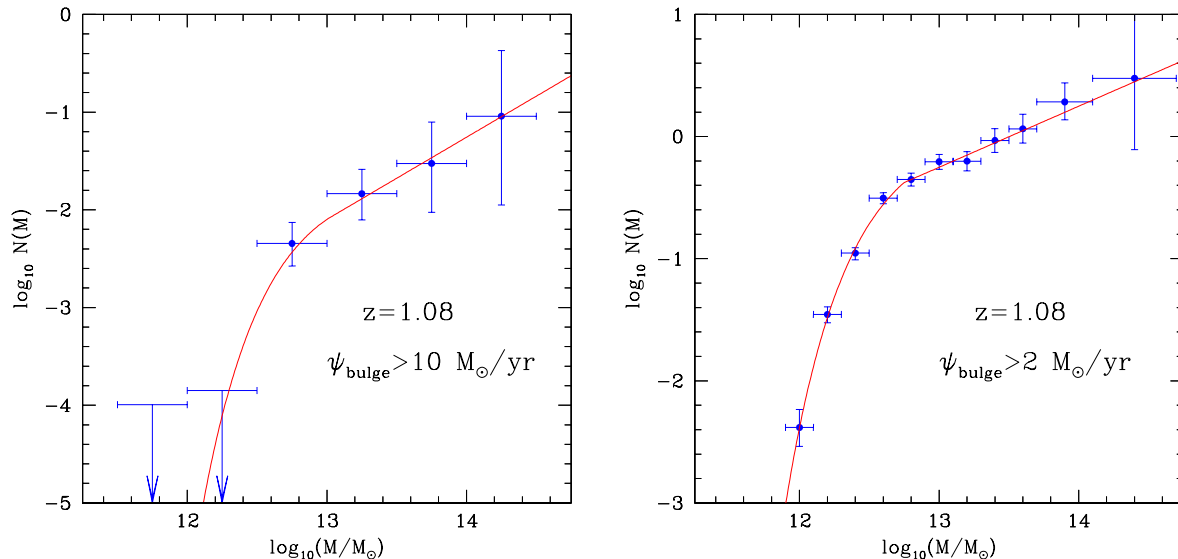


**Figure A1.** The halo occupation number of galaxies which at  $z = 1.08$  are actively forming stars in the bulge as obtained from semianalytic models of the GalICS collaboration (Hatton et al. 2003). The left panel refers to galaxies with a star formation rate in the bulge which is larger than  $10 M_{\odot} \text{ yr}^{-1}$ . These objects have nearly the same number density as quasars in our low-redshift sample. The right panel instead uses a threshold of  $\psi_{\text{bulge}} > 2 M_{\odot} \text{ yr}^{-1}$ . The corresponding galaxies are roughly 80 times more abundant than those used in the left panel. In both cases, the datapoints correspond to the estimated values of the halo occupation number, vertical errorbars mark the associated  $1\sigma$  uncertainties (assuming Poisson statistics for both the number of starforming galaxies and the number of haloes per bin), while the horizontal errorbars denote the size of the bins used to estimate  $N(M)$ . Arrows mark the upper limit for  $N(M)$  in the bins where we measure  $N = 0$ . The continuous lines show a fit to the data obtained by using the function in equation (A1). The adopted values for the parameters are listed in the main text.

refers to galaxies with a star formation rate in the bulge,  $\psi_{\text{bulge}}$ , which is larger than  $10 M_{\odot} \text{ yr}^{-1}$ . The choice of such a threshold for  $\psi_{\text{bulge}}$  is motivated by fact that the mean density of these objects ( $\sim 12 \times 10^{-6} h^3 \text{ Mpc}^{-3}$ ) is comparable with the mean density of our low-redshift quasar sample. In order to improve the statistics, in the right panel we also show the mean halo occupation number for galaxies with a bulge star formation rate,  $\psi_{\text{bulge}} > 2 M_{\odot} \text{ yr}^{-1}$ . In both cases, the halo occupation number is well approximated by a power law with a cutoff at small virial masses.

A number of functional forms can be used to describe the halo occupation number. For instance, if one only considers three adjustable parameters, the function

$$N(M) = N_0 \times \begin{cases} \left(\frac{M}{M_0}\right)^{\alpha} & \text{if } M \geq M_0 \\ \exp\left(1 - \frac{M_0}{M}\right) & \text{if } M < M_0, \end{cases} \quad (\text{A1})$$

very closely matches the results of the semi-analytical models in Fig. A1. In particular, for the left panel we find  $\alpha \sim 0.85$ ,  $\log_{10}(M_0/M_{\odot}) \sim 13$  and  $N_0 \sim 8 \times 10^{-3}$ . On the other hand,  $\alpha \sim 0.5$ ,  $\log_{10}(M_0/M_{\odot}) \sim 12.75$  and  $N_0 \sim 0.42$  for the right panel. Note that  $N_0$  gives the mean number of quasars contained in a halo of mass  $M_0$ . For  $M > M_0$  the halo occupation number scales as  $M^{\alpha}$ , while for  $M < M_0$  this is exponentially suppressed. This is in good agreement with equation (32) where a sharp cutoff replaces the exponential decline at small masses.

## A2 The scatter of $P_N(M)$

We can use the previously introduced samples of star-forming galaxies to study the scatter of the halo occupation number of rare objects at  $z \sim 1$ . Once again we rely on semi-analytic models for galaxy formation to get an insight on the possible behaviour of  $\Gamma(M)$  for quasars. We first note that there is not a single halo in the GalICS I sample which contains more than 1 galaxy with  $\psi_{\text{bulge}} > 10 M_{\odot} \text{ yr}^{-1}$  at  $z = 1.08$ . In other words, the data (within extremely large errorbars) are consistent with  $\Sigma^2 = 0$ . This is clearly an effect of the small number statistics (note that only 14 of these galaxies are present in the GalICS I sample and  $N(M) \ll 1$  – see Fig. A1). On the other hand, the results for  $\psi_{\text{bulge}} > 2 M_{\odot} \text{ yr}^{-1}$  are much more significant. In this case, the numerical results are well approximated by the function

$$\Gamma(M) = \left(\frac{M}{M_s}\right)^{\gamma_s} \left[1 + \left(\frac{M}{M_s}\right)^{\gamma_s}\right]^{-1} \quad (\text{A2})$$

which scales as a power law for  $M \ll M_s$  and approaches 1 for  $M \gg M_s$  (see Fig. A2). In agreement with previous studies (e.g. Scoccimarro et al. 2001; Magliocchetti & Porciani 2003), the scatter of  $P_N(M)$  is then strongly sub-Poissonian for haloes which, on average, contain less than 1 object, and nearly Poissonian for larger haloes. Similar results have been obtained for local galaxies by using different semi-analytical models (e.g. Sheth & Diaferio 2001; Berlind & Weinberg 2002) and hydrodynamical simulations (Berlind et al. 2003).

In order to avoid the introduction of additional free parameters, it would be ideal to express  $\gamma_s$  and  $M_s$  in terms

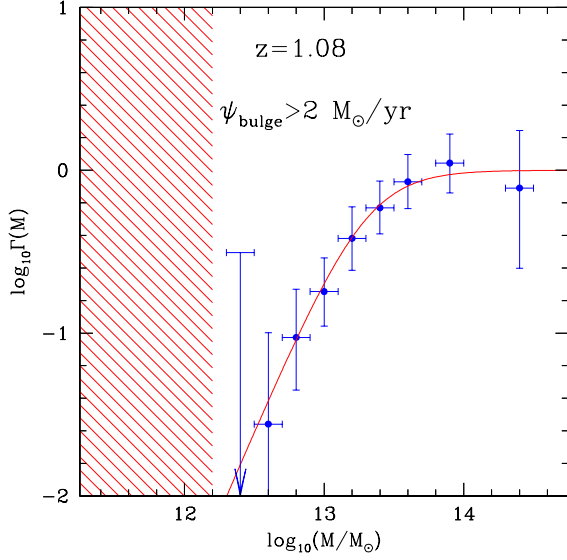


**Figure A2.** As in Fig. A1 but for the function  $\Gamma(M)$ . The fitting function represented with a continuous line is given in equation (A2). The best-fitting parameters are listed in the main text. The shaded region indicates the mass range where the function  $\Gamma$  is totally undetermined.

of  $\alpha$ ,  $M_0$  and  $N_0$ . We note that the data in Fig. A2 are well fitted by  $\gamma_s \sim 2$  and  $\log_{10}(M_s/M_{\odot}) \sim 13.3$ . We find that, adopting  $N(M_s) = 0.75$  as an operative definition for  $M_s$ , equation (A2) with  $\gamma_s = 2$  accurately describes a wide range of synthetic datasets.